MLM-2892
UC-4 and UC-22

Mound Facility Activities in Chemical and Physical Research: July-December 1981

Issued: May 3, 1982

MLM--2892

DE82 014717

MOUND FACILITY
Miamisburg, Ohio 45342

operated by
MONSANTO RESEARCH CORPORATION
a subsidiary of Monsanto Company

for the
U. S. DEPARTMENT OF ENERGY

Contract No. DE-AC04-76-DP00053

Foreword

This report is issued semiannually by MRC-Mound. Under the sponsorship of the DOE Division of Basic Energy Sciences, Mound is responsible for research in the physical sciences to further the progress of science and technology in the public interest. This report is submitted by W. T. Cave, Director of Nuclear Operations, and R. E. Vallee, Manager of Technology Applications and Development, from contributions prepared by W. M. Rutherford, Science Fellow (Thermal Diffusion); W. L. Taylor, Science Fellow (Gas Dynamics and Cryogenics); G. L. Silver, Science Fellow (Separation Chemistry); L. J. Wittenberg, Leader, Metal Hydride Research; and from members of the Isotope Separation Section: W. R. Wilkes, Isotope Separation Manager; E. D. Michaels, Leader, Isotope Separation Engineering; and B. E. Jepson, Senior Research Specialist, Metal Isotope Separation Research and Development.

These reports are not intended to constitute publication in any sense of the word. Final results either will be submitted for publication in regular professional journals or will be published in the form of MLM topical reports.

Previous reports in this series are:

MLM-2198	MLM-2555
MLM-2241	MLM-2590
MLM-2296	MLM-2654
MLM-2354	MLM-2727
MLM-2414	MLM-2756
MLM-2450	MLM-2809
MLM-2506	MLM-2884

Contents

I. Low temperature research

Page

REACTION RATES OF DEUTERIUM-TRITIUM MIXTURES. 6

The D_2+T_2 reaction rate experiments have shown that the rate controlling mechanism is in the gas phase. The reciprocal reaction time goes to zero as the pressure goes to zero. Trace amounts of CT_4 (~0.02%) in some experiments act as an inhibitor for the reaction.

THERMOMETRY 7

In using a platinum thermometer in the region of 13 to 30 K, an independent method of analyzing the Rosemont calibration data indicates a cusp in the calibration function at 18 K.

EVALUATION OF HYDROGEN SECOND VIRIALS USING ANGLE-DEPENDENT POTENTIAL FUNCTIONS . . 8

A code has been developed to calculate second virials using angle-dependent potential functions in the semi-classical Wang Chang formalism. The calculation involves quadruple numerical integrations. Comparisons have been made using the Wang Chang and the Etters potential functions.

II. Separation research

LIQUID PHASE THERMAL DIFFUSION. 14

The separation of isotopically substituted dimethyl zinc was determined in a 45 cm liquid phase thermal diffusion column. The $ZnCH_4^+$ fragment was found to be best for the mass spectrometric determination of the relative concentrations of the zinc isotopes. The separation factors for the ^{64}Zn-^{68}Zn pair ranged from 1.18 to 1.20.

A continuous flow capillary apparatus was constructed for measurements of liquid phase viscosities. Preliminary measurements of the viscosity of methyl chloride at 35 atm gave results in good agreement with the very old (1894) data of de Haas but the values are much lower than those published more recently.

CALCIUM ISOTOPE SEPARATION. 18

Work on the separation of calcium isotopes by liquid phase thermal diffusion of aqueous calcium nitrate solutions continued. Equilibrium separation factors for the $^{40}Ca/^{48}Ca$ pair in the solvent counterflow apparatus ranged from 1.39 at 1.3 wt % $Ca(NO_3)_2$ to 1.15 at 35 wt %. Time constants for the separations were 4 to 8 days.

Page

CHEMICAL EXCHANGE 22

The heterogeneous exchange rate kinetics of calcium ions with resin-bound 222B cryptand were investigated. The exchange rate found was too slow to form the basis of a calcium isotope enrichment process; however, some improvements are possible.

MUTUAL DIFFUSION. 23

Mutual diffusion coefficients of Xenon-Argon are reported for a temperature range from approximately 350 to 1250 K. These results agree with the Marrero and Mason correlation derived from diffusion and molecular beam data. Viscosity and thermal diffusion data were also mutually consistent with the results to within ∿5% at high temperatures and better than ∿2.5% at the lower temperatures. A comparison with theoretical diffusion coefficients calculated from recently proposed intermolecular potentials is made for the He-, Ne-, and Xe-Ar systems.

MOLECULAR BEAM SCATTERING 29

The molecular beam triple-pumped detector system has been installed on the beam chamber without the quadrupole detector housing for initial testing of the large rotary vacuum seal. The velocity selector test system has been upgraded to provide higher detection sensitivity.

Total cross sections which were computed theoretically from seven He-Ar interatomic potentials given in the literature were compared to the experimental data. The Dymond-Alder (DA) potential was found to best represent the data.

CALCIUM ISOTOPE ENRICHMENT. 31

A description of the calcium chemical exchange experimental system and experiments is presented. The data obtained from flooding experiments with a Karr reciprocating plate column are compared to a published model. This model and other correlations are used to estimate HTU's for the calcium isotope chemical system. Results indicate that Karr column performance is adequate for the larger portions of a calcium isotope cascade.

III. Metal hydride studies

Page

JAHN-TELLER RESONANCE STATES IN THE Vb METAL HYDRIDES: STATIC AND DYNAMIC CONSEQUENCES 39

A Hamiltonian with a localized Jahn-Teller electron-phonon interaction plus a band-coupling term belonging to a metal cluster state adjacent to interstitial hydrogen in the Vb metals is presented. It is shown that in a low-frequency approximation, this Hamiltonian is analogous to the Anderson Hamiltonian for magnetic impurities in metals. The role of hydrogen in triggering the Jahn-Teller instability is explained in the context of the Hartree-Fock solutions of the low-frequency Hamiltonian, using a 'phase diagram' in the Hartree-Fock parameter space. Anelastic relaxation mechanisms are described, and an elastic susceptibility expression is derived and compared with an observed elastic relaxation. One of the relaxation mechanisms is analogous to the Kondo effect, suggesting that a logarithmic singularity might be observed in a low-temperature resistivity study.

References 47

Distribution 51

I. Low temperature research

Reaction rates of deuterium-tritium mixtures

G. T. McConville, D. A. Menke, and R. E. Ellefson

The rate of reaction experiments of D_2+T_2 described in previous progress reports [Ref. 1,2] are continuing and have yielded some interesting results. In the last report, we showed that, when T_2 was put into the mixing chamber 24 hr in advance of the D_2, the reaction rate was three times slower than when the two gases were put into the mixing chamber at nearly the same time. Two questions arose: Was the rate controlling reaction due to the gas phase reaction or to a catalytic reaction on the surface of the mixing chamber? And what determined the difference in the two kinds of experiments?

The previous mixing experiments using 30% T_2 were done at pressures of 500, 300, and 150 torr. New measurements were done at 40 and 20 torr to determine whether the reaction was a gas phase reaction. The time, t_1, for the reaction to go to 1/e in the 40 torr experiment was 125 min, and in the 20 torr experiment was 280 min. If one plots $1/t_1$ as a function of pressure for the five experiments, as shown in Figure I-1, one sees that $1/t_1$ goes to zero as the pressure goes to zero, indicating that the reaction is indeed a gas phase reaction.

The pressure dependence is divided into two regions. In the pressure independent region, where all of the energy of the β^- is dissipated in the gas, the ratio of the forward reaction rate to the reverse rate, K_f/K_r, is independent of pressure and is expressed only in terms of time dependent mole fractions. On the basis of early experiments measuring β^- track lengths in hydrogen gas [Ref. 3], a rough calculation of the range, R in cm, of the maximum energy β^- in a gas of hydrogen isotopes gives $R = 1300/P$ with pressure in torr. Thus, when R equals the cell radius of 3.8 cm, P is ∿340 torr, which is close to the break in the curve in Figure I-1. As the pressure is reduced below this value, a larger fraction of the β^- energy is absorbed in the cell wall leading to a slower rate of DT production.

Since the pressure dependence of the reaction rate indicates a gas phase reaction, the impurity content of the samples was studied closely to see whether leaving the T_2 in the mixing chamber 24 hr produced

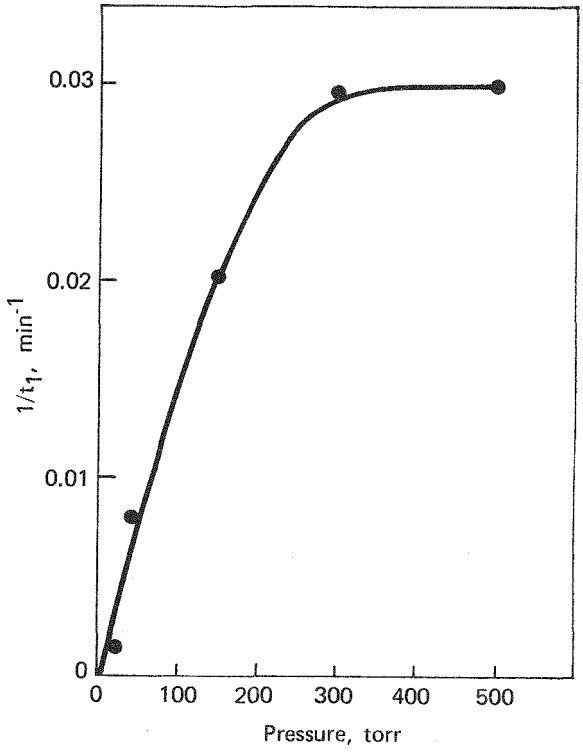

FIGURE I-1 - Pressure dependence of the reaction time t_1 for 30% T_2 mixtures at 295 K.

an impurity that could act as an inhibitor for the reaction. The mass spectrometric analysis indicated that the initial D_2 and T_2 were very clean, with ~0.2% HD the only detectable impurity in the D_2 and only 3 to 4% ^3He detectable in the T_2 as it aged over the course of the experiments. The only impurity we found was CT_4 in the T_2 that was allowed to set in the mixing cell for 24 hr. Before the D_2 was added, 0.035% CT_4 was found in the T_2. Adding the D_2 pushed the CT_4 concentration below the detectable limit of the mass spectrometer. A second experiment with T_2 in the cell 48 hr in advance of mixing produced a slower reaction yet, and 0.053% CT_4 was detected in the T_2. If one assumes there is no CT_4 when the D_2 and T_2 are mixed at the same time, Figure I-2 shows that the t_1 increases linearly as the CT_4 concentration in the sample increases. CT_4 appears to be a strong inhibitor of the reaction.

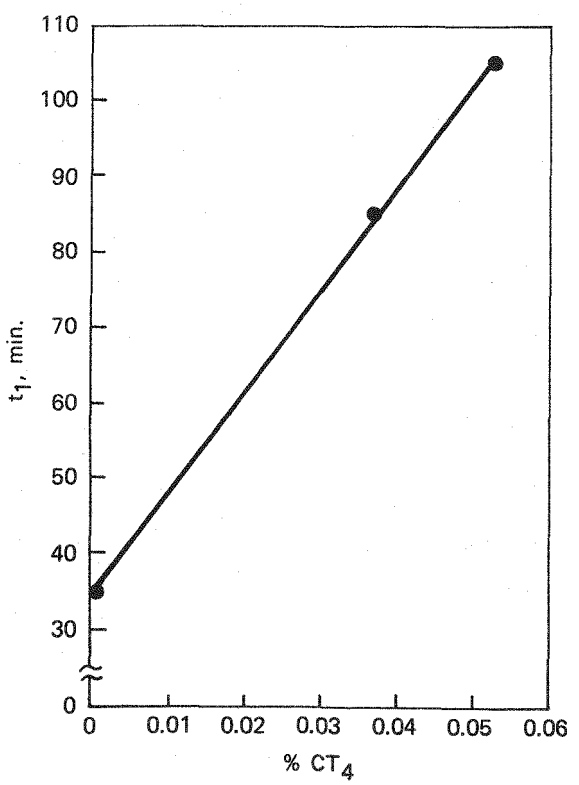

FIGURE I-2 - Concentration dependence of the reaction time t_1 as a function of CT_4 in the T_2 before mixing.

Reaction rate experiments using 30% T_2 have been started at 77 K (liquid nitrogen temperature). The rate is very slow and therefore the value of t_1 obtained at P = 75 torr, corresponding to the same density as the 300 torr experiments at 295 K, has a large uncertainty. The preliminary value is 660 $\pm$ 50 min. This is about a factor of 20 slower than the 295 K measurements. More experiments at 77 K are planned. The 295 K results have been submitted for publication.

Thermometry

G. T. McConville and D. A. Menke

In a previous report [Ref. 4] a comparison was made between the calibration of a Rosemont Type 146L platinum thermometer from Rosemont Engineering, and temperature determined from the measured vapor pressure of neon-20 and deuterium + 0.84% HD corresponding to the deuterium used in the vapor pressure measurements of Grilly [Ref. 5]. The analysis indicated that the oscillation that showed up in the fitting of the neon vapor pressure data [Ref. 4] resulted from the Rosemont calibration. We now can show the cause of the oscillation in a way that is independent of the vapor pressure data. Rosemont publishes a table of resistance ratios [Ref. 5], R_T/R_O, as a function of T for a "typical," pure, annealed, strain-free platinum thermometer, where R_T is the resistance at a temperature T and R_O is the resistance at 0°C. The entries are in one degree intervals down to -260°C (13.15 K), with one additional point at -268.95°C (4.20 K). Taking the calibration points for our thermometer #2788 from the table supplied by Rosemont, we can determine the deviation

from the standard table by constructing a curve from the following expression:

$$R_e(0°C) = R_T(\text{cal})\left(\frac{R_O}{R_T}\right)(\text{standard table})$$

We would expect the curve to be a smooth monotonic function of T. Figure I-3 represents a curve for thermometer #2788, and it is not as we expected. The oscillation in the vapor pressure representation is due to the cusp in the figure at about 18 K. This variation turns out to be within the stated accuracy of 0.02 K given by Rosemont Engineering.

The effort to improve the accuracy of our thermometry in the region of 13 to 27 K was to obtain accurate measurements of the effect of HD on the vapor pressure of D_2. The impurity HD in D_2 is virtually impossible to eliminate. The partial pressure of 0.84 HD in D_2 goes from 0.55 torr at 16 K to 9.52 torr at 23.67 K [Ref. 6]. Thus, if one were to try to determine temperature using D_2 free of HD and Grilly's equations, his determinations would range from 17 mK too high at 16 K to 14 mK too high at 23.67 K.

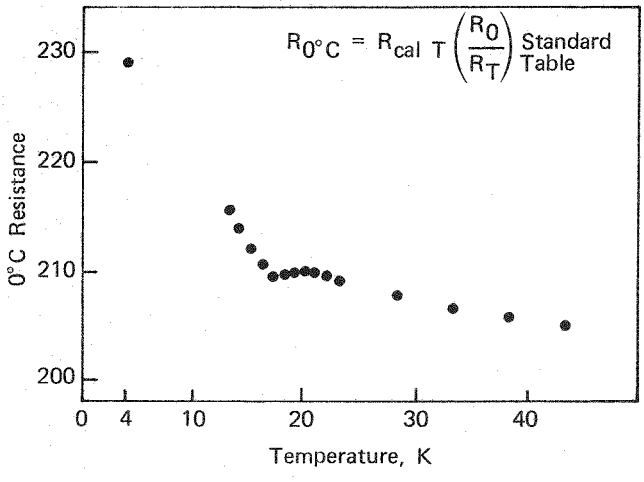

FIGURE I-3 - Effective 0°C resistance from the calibration points of thermometer #2788.

The differential measurements [Ref. 7] of nD_2 against eD_2 with HD concentrations of 0.18% and 0.14%, respectively, were made taking considerable care to get the same amount of sample in each bulb. The nD_2 + 0.84% HD measurement was done with sample only in one bulb as was the case with the ^{20}Ne. Thus, when the nD_2 + 0.18% HD was measured at the same pressures, the purer D_2 was 0.007 $\pm$ 0.003 mK in the liquid region, but in the solid region the difference turned negative to -0.01 K at 16.2 K. Temperature gradients in the present cryostat preclude more than a qualitative comparison to the partial pressure of HD calculated from Wooly, Scott, and Brickwedde. This work has been accepted for presentation at the 6th Symposium on Temperature.

Evaluation of hydrogen second virials using angle-dependent potential functions

G. T. McConville and R. E. Miers

Calculation of the second virial coefficient can be divided into three regimes: purely classical formalism, a complete quantum calculation, and an expansion in even powers of Planck's Constant to span the intermediate temperature region between the first two cases. The third expansion was first given by Wigner [Ref. 8] and Kirkwood [Ref. 9] and is useful where quantum effects are beginning to appear, but a

full quantum calculation would require the evaluation of a prohibitive number of phase shifts. Although the expansion was originally formulated for spherical molecules, the extension to nonspherical molecules, specifically hydrogen, was made in the 1944 University of Michigan thesis of Wang Chang. The formalism is complicated and few attempts have been made to calculate hydrogen virials using it.

The form of the classical second virial for a diatomic gas is given by:

$$B_{Cl} = \frac{N}{4} \int_0^\infty r^2 dr \int_0^\pi \sin\theta_1 d\theta_1 \int_0^\pi \sin\theta_2 d\theta_2 \int_0^{2\pi} d\phi \left[1 - e^{\frac{-V(r_1\theta_1,\theta_2,\theta)}{KT}}\right] \quad (1)$$

where

θ_1 and θ_2 are the angles the axes of the two molecules makes with the line joining these centers, and

ϕ is the angle made by the two planes, each of which contains the axis of one molecule and the line joining the two centers.

The form of the total second virial in terms of the Wigner-Kirkwood expansion is:

$$B_T = B_{Cl} + \frac{\hbar^2}{m} B_1 + \left(\frac{\hbar^2}{m}\right)^2 B_2 + B_0 \quad (2)$$

where B_0 is the ideal gas contribution when these particles obey either Fermi-Dirac or Bose Einstein statistics, and B_1 and B_2 were given by Wang Chang as:

$$B_1 = \frac{N}{4} \int_0^\infty \int_0^\pi \int_0^\pi \int_0^{2\pi} r^2 dr \sin\theta_1 d\theta_1 \sin\theta_2 d\theta_2 d\phi \; e^{\frac{-V}{KT}} \left[\frac{1}{12K^3T^3}\left(\frac{\partial V}{\partial r}\right)^2 + \frac{1}{24I/mK^2T^3}\left[\sum_\alpha \left(\frac{\partial V}{\partial \theta_\alpha}\right)^2 + \sum_\alpha \csc^2\theta_\alpha \left(\frac{\partial V}{\partial \phi}\right)^2\right]\right] \quad (3)$$

and

$$B_2 = \frac{N}{4} \int_0^\infty \int_0^\pi \int_0^\pi \int_0^{2\pi} r^2 dr \sin\theta_1 d\theta_1 \sin\theta_2 d\theta_2 d\phi \; e^{\frac{-V}{KT}} \left[-\frac{1}{120K^4T^4}\left[\left(\frac{\partial^2 V}{\partial r^2}\right)^2 + \frac{2}{r}\left(\frac{\partial V}{\partial r}\right)^2 - \frac{5}{3KT}\left(\frac{\partial V}{\partial r}\right)^2 \frac{\partial^2 V}{\partial r^2} + \frac{5}{12(KT)^2}\left(\frac{\partial V}{\partial r}\right)^4\right] - \frac{K_3}{2I/mK^4T^4} - \frac{1}{480I^2/m^2K^4T^4}\left(K_3 - \frac{5}{3}\frac{1}{KT}K_4 + \frac{5}{12}\frac{1}{(KT)^2}K_5\right)\right] \quad (4)$$

where K_3, K_4, K_5 are complex functions of the angle variables and are given in full in the Wang Chang thesis. B_1 and B_2 are usually broken into two parts: B_{1t} being the first term containing $\partial V/\partial r$ and B_{1r} being the remaining terms containing the derivatives of V with respect to the angles. When Wang Chang evaluated the above integrals, she used a rather simple angle dependent potential, which is not really a description of the hydrogen potential, of the form:

$$V = A/r^{12}(\cos^2\theta_1 + \cos^2\theta_2) - B/r^6$$

This form is convenient because a transformation of $X_1^2 = \cos^2\theta_1$ produces integrals of the form:

$$\int_1^1 F(X_1) e^{-X_1^2} dX_1$$

which can be evaluated in terms of error functions and reduces the evaluation of B_1 and B_2 to only one numerical integration over r. Wang Chang evaluated B_{Cl}, B_{1t}, B_{1r},

and B_{2r} for this potential. She did not calculate B_{2t} and thus made calculations down to only 123 K. As a test, we have reproduced the calculations of Wang Chang and also calculated B_{2t}.

The comparison of Wang Chang's results (which were done by hand) and the present results are shown in Table I-1. Except for the 423 K value for B_{Cl}, there is quite good agreement. A comparison with experimental data between 60 and 423 K is shown in Figure I-4 for high temperatures and in Figure I-5 for low temperatures. At no temperature is there good agreement. The lack of agreement can be attributed to the Lennard-Jones form Wang Chang used for the radial part of the potential function.

Table I-1 - COMPARISON OF PRESENT CALCULATIONS TO THOSE OF WANG CHANG

	B_{Cl}		B_{1t}		B_{1r}	
Temperature,(K)	WC	Present	WC	Present	WC	Present
523		15.39		0.57		0.06
423	15.22	14.59	0.64	0.78	0.08	0.09
373	14.06	13.94	0.97	0.88	0.12	0.11
323	13.15	13.01	1.13	1.06	0.15	0.14
273		11.58		1.33		0.19
223	9.49	9.41	1.76	1.74	0.28	0.27
173	5.68	5.61	2.58	2.50	0.46	0.45
138		0.96		3.51		0.71
123	-3.06	- 1.99	4.23	4.21	1.00	0.90
113		- 4.47		4.28		1.08
98		- 9.30		6.10		1.49
90		-12.66		7.06		1.81
80		-17.98		8.71		2.40
75		-21.27		9.81		2.81
70		-25.12		11.16		3.41
60		-35.21		15.12		4.99

	B_{2t}	B_{2r}		B_{total}	
Temperature, (K)	Present	WC	Present	WC	Present
523	- 0.08		-0.008		15.96
423	- 0.13		-0.012	15.94	15.31
373	- 0.17		-0.018	15.15	14.77
323	- 0.24	-0.02	-0.026	14.43	13.98
273	- 0.35		-0.093		12.75
223	- 0.56	-0.07	-0.078	11.53	10.86
173	- 1.03	-0.14	-0.169	8.72	7.54
138	- 1.82		-0.347		3.14
123	- 2.44	-0.42	-0.506	2.17	0.32
113	- 3.05		-0.672		- 2.12
98	- 4.47		-1.09		- 7.07
90	- 5.64		-1.48		-10.67
80	- 7.85		-2.26		-16.71
75	- 9.45		-2.88		-20.67
70	-11.55		-3.74		-25.56
60	-18.34		-6.80		-39.80

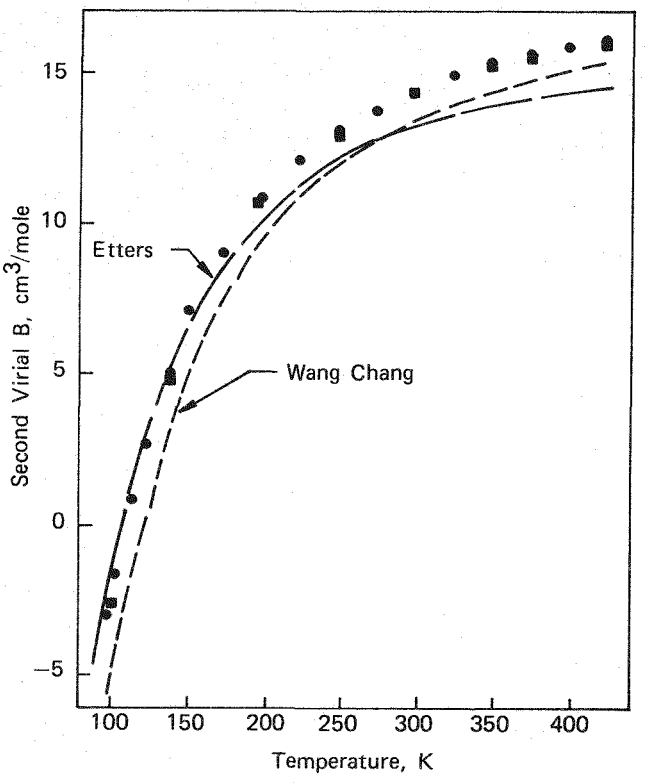

FIGURE I-4 - Temperature dependence of hydrogen second virial compared with calculations using Wang Chang's and Etters's potential functions between 100 and 423 K.

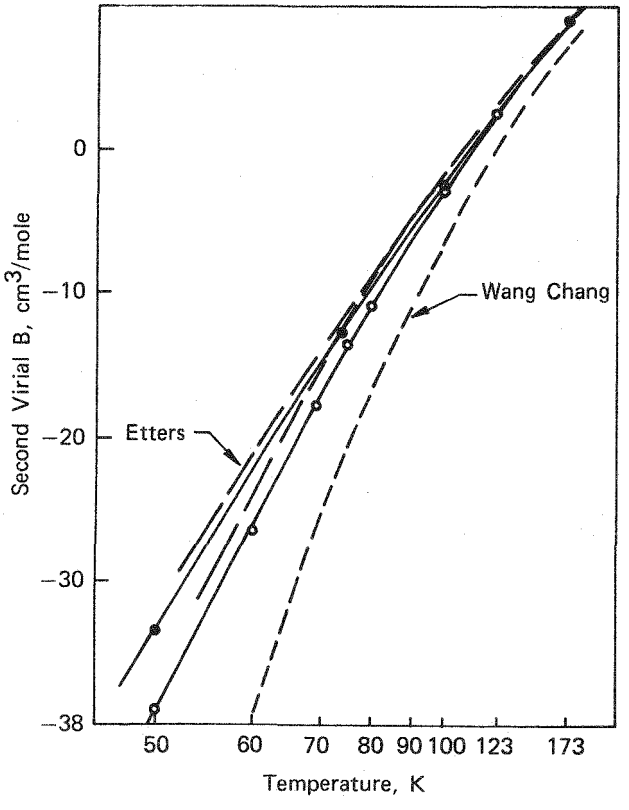

FIGURE I-5 - Temperature dependence as in Figure 4 between 60 and 173 K.

Recently, a calculation of the second virial of hydrogen has appeared using a much more complex potential function proposed by Etters, et al. [Ref. 10]. They also calculated the second virial using the Wang Chang formalism, but the complexity of the angular dependence of the potential required a numerical integration for all four integrals. The form of their potential is an exp-6-8 with 5 terms making up the repulsive part. These terms correspond to different orientations of a pair of molecules, giving:

$$U_l(r_1,\theta_1\ \theta_2,\phi) = \sum_{l=1}^{\pi} A_l(r)B_l(\theta_1,\theta_2,\phi)$$

where

$$A_1(r) = \exp[b_x(r)],$$

$$A_2(r) = r^2 \exp[b_\pi(r)] - \exp[b_x(r)],$$

$$A_3(r) = A_3(r)/r^3,$$

$$A_4(r) = \exp[b_T(r)] - \exp[b_x(r)] - A_2(r),$$

$$A_5(r) = 2[\exp b_L(r) - \exp b_\pi(r)] - 5.4A_4(r) - 4A_2(r),$$

$$A_6(r) = 3.158 \times 10^5 C(r) r^{-2},$$

$$A_7(r) = 3.158 \times 10^5 C(r) r^{-2},$$

$$A_8(r) = -3.663 \times 10^7 C(r) r^{-2},$$

For $r < 5$ a.u.:

$$b_L(r) = 15.4381 - 1.7532r,$$

$$b_\pi(r) = 13.8444 - 1.2827r - 0.0470916r^2,$$

$$b_T(r) = 13.6828 - 1.10567r - 0.078402r^2,$$

$$b_x(r) = 13.5979 - 1.15432r - 0.06737r^2,$$

and for $r > 5$ a.u.:

$$b_L(r) = 16.2815 - 1.9219r,$$

$$b_\pi(r) = 17.04057 - 2.29122r + 0.026851r^2,$$

$$b_r(r) = 15.40474 - 1.84207r,$$

$$b_x(r) = 15.4541 - 1.8624r.$$

The angular dependent terms B_l are:

$$B_1 = 1,$$

$$B_2 = \cos^2\theta_1 + \cos^2\theta_2,$$

$$B_3 = (\cos\theta_1 \cos\theta_2 + \sin\theta_1 \sin\theta_2 \cos\phi)^2$$

$$B_4 = \cos^2\theta_1 + \cos^2\theta_2 + 0.7\cos\theta_1\cos\theta_2 (\cos\theta_1\cos\theta_2 + \sin\theta_1 \sin\theta_2\cos\phi),$$

$$B_5 = 1/2\cos^2\theta_1\cos^2\theta_2,$$

$$B_6 = 0.04805[1 - 5(\cos^2\theta_1 + \cos^2\theta_2 + 3\cos^2\theta_1\cos^2\theta_2) + 2(\sin\theta_1\sin\theta_2\cos\phi + 4\cos\theta_1\cos\theta_2)^2],$$

$$B_7 = -0.2002(\sin\theta_1\sin\theta_2\cos\phi - 2\cos\theta_1\cos\theta_2)^2 - 1.672(\cos^2\theta_1+\cos^2\theta_2)-11.133,$$

$$B_8 = 1.0$$

The calculations involving this potential in Equations 1 through 4 are quite complex because they involve four nested numerical integrations. A comparison of the present calculations to those of Etters, et al. (Table I-2) shows the worst agreement is in B_{1r}. Etters' values appear to go through a maximum at about 90 K which does not appear in our calculations or Wang Chang's. We have not calculated B_{2r} yet. A comparison of B_{Total} shows poor agreement at low temperature because of the differences in B_{1r}. As shown in Figures I-4 and I-5, the difference between J = 0 (para H_2) and normal hydrogen only becomes apparent at temperatures below 100 K. The difference that is calculated is about that seen experimentally but, again, the radial part of the potential does not give a good description of the higher temperature data.

Calculations are in progress using our HFD radial function [Ref. 11] and a quadrupolar angular term. This function is known to give a good description for the J=0 data (para H_2). The purpose of these calculations is to produce a transition to the very low temperature calculations of the second virial in terms of averaged phase shifts calculated from the solution of coupled Schrodinger equations. This program of calculations is also under way.

Table I-2 - COMPARISON OF PRESENT CALCULATIONS TO THOSE OF ETTERS, et al.

	B_{C1}		B_{1t}		B_{1r}	
Temperature, (K)	Etters	Present	Etters	Present	Etters	Present
523	14.42	14.25	0.35	0.35	0.049	0.046
423	13.95	13.80	0.47	0.47	0.075	0.070
373	13.48	13.37	0.56	0.56	0.098	0.089
323	12.73	12.70	0.69	0.69	0.13	0.12
273	11.65	11.63	0.88	0.89	0.18	0.16
223	9.79	9.84	1.19	1.21	0.27	0.24
173	6.48	6.64	1.76	1.80	0.41	0.39
138	2.33	2.62	2.52	2.59	0.57	0.58
113	- 2.55	- 2.14	3.49	3.61	0.70	0.84
98	- 6.90	- 6.40	4.43	4.60	0.74	1.10
90	- 9.92	- 9.37	5.21	5.31	0.74	1.29
80	-14.71	-14.06	6.30	6.53	0.64	1.60
70	-21.10	-20.36	8.01	8.29	0.36	2.08

	B_{2t}		B_{2r}		B_{total}	
Temperature, (K)	Etters	Present	Etters	Present	Etters	Present
523	- 0.002	0.001	0.02	-	14.86	14.68
423	- 0.004	0.001	0.02	-	14.52	14.36
373	- 0.005	0.001	-0.01	-	14.15	14.12
323	- 0.008	0.001	-0.02	-	13.59	13.51
273	- 0.013	- 0.001	-0.04	-	12.70	12.65
223	- 0.022	- 0.007	-0.06	-	11.23	11.22
173	- 0.046	- 0.037	-0.10	-	8.52	8.68
138	- 0.110	- 0.113	-0.14	-	5.22	5.25
113	- 0.244	- 0.283	-0.33	-	1.23	1.70
98	- 0.454	- 0.530	-0.41	-	- 2.39	- 2.06
90	- 0.663	- 0.764	-0.46	-	- 4.96	- 3.89
80	- 1.121	- 1.206	-0.55	-	- 9.16	- 8.25
70	- 2.024	- 2.199	-0.71	-	-15.14	-13.46

II. Separation research

Liquid phase thermal diffusion

W. M. Rutherford

THERMAL DIFFUSION OF DIMETHYL ZINC

Metal alkyls are potentially useful working fluids for the liquid phase separation of metal isotopes. A series of experiments was set up, therefore, to test the possiblity of using dimethyl zinc as a fluid for the separation of zinc isotopes. Dimethyl zinc is a volatile, pyrophoric fluid; however, it seems to be reasonably stable in the typical operating temperature range of the liquid phase thermal diffusion columns (15-164°C).

Electronic grade dimethyl zinc was degassed at liquid nitrogen temperature and transferred to the feed system of the 45 cm thermal diffusion research column (Fig. II-1), which had been assembled to a hot to cold wall spacing of 254 μm. After the evacuated column had been heated to normal operating conditions (6.8 atm steam, 15°C cooling water) the charge of dimethyl zinc was admitted to the column working space under a pressure of 35 atm.

The fluid was kept in the column under these conditions for 22 days, during which time no gross decomposition of the material was observed. Vapor phase samples for mass spectrometric analysis were taken at intervals of several days, but problems associated with getting a clean, stable, representative sample into the mass spectrometer were not completely worked out until the 14th day of the experiment.

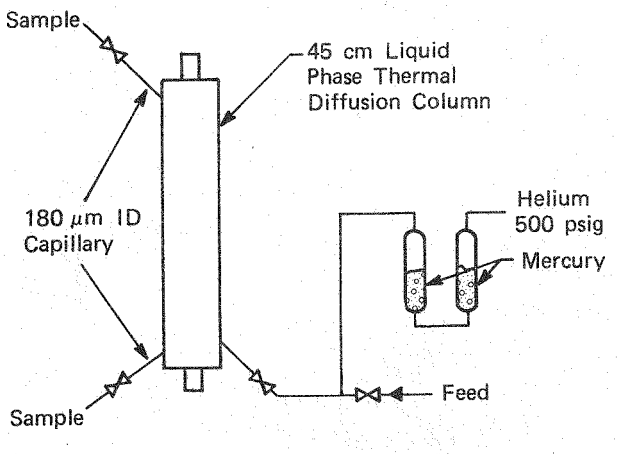

FIGURE II-1 - Apparatus for liquid phase isotopic separation of dimethyl zinc.

We found the $ZnCH_4^+$ fragment to be best for determining the relative amounts of the several zinc isotopes. The results, expressed in terms of the apparent ratio of ^{68}Zn to ^{64}Zn, are given in Table II-1 along with the separation factors calculated therefrom.

Table II-1 - LIQUID PHASE THERMAL DIFFUSION OF DIMETHYL ZINC

Time (days)	Ratio: mass 83 peak to mass 79 peak		Separation Factor
	Top	Bottom	
14	0.3203	0.3784	1.18
17	0.3337	0.3988	1.20
22	0.3369	0.3966	1.18

The separation factors appear to be large enough to support a practical scale separation process; however, more data are needed to establish the thermal diffusion factor of the system and to determine the kinetics of decomposition of the compound.

VISCOSITY OF METHYL CHLORIDE

The theoretical expressions for the thermal diffusion column coefficients are complicated functions of the dimensions and operating conditions of the column and the physical properties of the working fluid. To make accurate predictions of the column coefficients it is necessary, therefore, to have accurate values for the density, viscosity, diffusion coefficient, thermal conductivity, and thermal diffusion factor as functions of temperature.

The results of liquid phase thermal diffusion experiments with methyl chloride have been presented in previous reports. Interpretation of the separation data in terms of theory was tenuous because the published viscosity data for liquid phase methyl chloride are conflicting. There were large discrepancies among the several observers and much of the data seems to be unreasonable with respect to the other chlorinated methanes and in comparison to values obtained from recommended correlation methods.

The initial transport coefficient is proportional to the reciprocal of the viscosity, and the convective remixing coefficient depends on the inverse square of the viscosity. Thus, errors in the viscosity have a significant effect on the theoretical interpretation of the experimental results.

A high pressure viscometer was constructed to enable us to measure the viscosity of methyl chloride in the temperature range of interest for the thermal diffusion work. The apparatus (Fig. II-2) is a steady flow capillary device similar in concept to the devices used by Flynn, Hanks, Lemaire and Ross [Ref. 1], by Kao, Ruska and Kobayashi [Ref. 2] and by Sun and Storvick [Ref. 3]. The capillary is a 141.78 mm length of fused silica chromatographic tubing with a nominal inside diameter of 200 μm supported inside a section of 3.2 mm o.d., 0.5 mm i.d. stainless steel tubing. Flow through the capillary is established by the movement of two identical piston injectors driven by a synchronous motor through an adjustable gear train.

The pressure differential across the capillary is measured by a Sensotec wet/wet differential pressure transducer with a

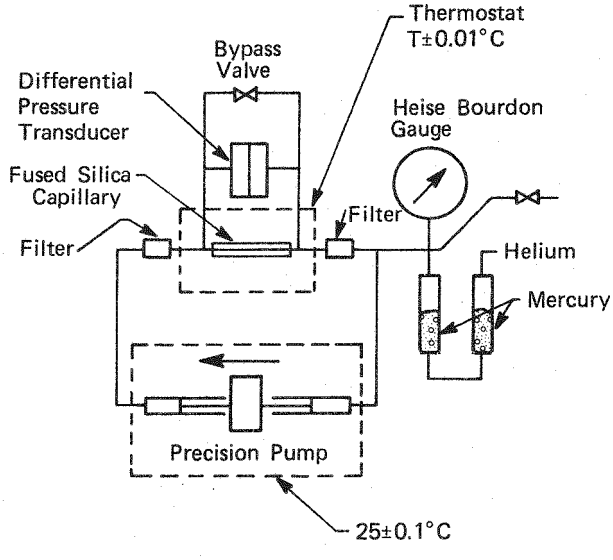

FIGURE II-2 - Simplified schematic diagram of viscosity apparatus.

full-scale range of ± 0.5 psid and a nominal accuracy of ± 0.5%. Total pressure is measured with a 2000 psig Heise bourdon tube gauge accurate to ± 1 psig.

Water jackets on the piston injectors maintain the temperature at 25 ± 0.1°C, and the temperature of the capillary is established by a water or oil bath within a tolerance of ± 0.01°C.

The modified Poiseuille equation for the viscosity in terms of the experimental parameters is:

$$\eta = \eta_p - mX$$

where

$$\eta_p = \frac{\pi a^4 \Delta p}{8 Q L_{eff}}$$

$$X = \frac{\rho Q}{8 \pi L_{eff}}$$

where

a = capillary radius
Δp = pressure difference across the capillary
Q = volumetric flow rate
m = Hagenbach factor
L_{eff} = effective length of capillary
ρ = density of fluid

The slip correction, the Couette correction, and the thermal expansion of the capillary are negligible for the conditions of the experiments reported here. A value of 1.18 was assumed for m in keeping with the results reported in References 1 and 3.

The apparatus was calibrated with compressed helium gas at 25°C using a reference value from Kestin, Ro, and Wakeham [Ref. 4]. Viscometer data at 4.382 atm were used to establish the value of the constant:

$$C = a^4/L_{eff}$$

with the results given in Table II-2.

The response of the differential pressure transducer is somewhat influenced by the total pressure in the system. As an interim measure, in lieu of an explicit calibration of the instrument, a pressure correction factor correlation was developed from helium measurements at 25°C in the pressure range from 11 to 103 atm, again using standard values of Kestin, Ro and Wakeham as reference. The maximum correction was found to be 2.4% at the maximum working pressure of the system, 100 atm.

As a check on system response, we determined the viscosity of nitrogen at 25°C in the pressure range from 4.38 to 69.03 atm. The results are given in Table II-3 along with values interpolated from Kestin and Leidenfrost [Ref. 5]. The differences relative to the Kestin and Leidenfrost data are substantially smaller than one would expect based on the precision of our measurements, which is estimated to be ± 1%.

Experimental data have now been gathered for methyl chloride at 35 atm and at temperatures of 20, 40, 60, and 90°C. Significant pressure fluctuations were observed during the liquid phase displacements. In order to get satisfactory precision, we used a laboratory computer to record and average the pressure measurements during the displacement process. A typical standard deviation of ± 1% was obtained for approximately 150 readings of the pressure differential.

Results of the measurements are given in Table II-4 and in Figure II-3. Figure II-2 also contains results abstracted from the literature. Our results agree quite well with those of de Haas [Ref. 6], but they

are substantially below the measurements of Stakelbeck [Ref. 7] and Benning and Markwood [Ref. 8], and somewhat below those of Awbery and Griffiths [Ref. 9].

Table II-2 - CALIBRATION OF EXPERIMENTAL VISCOMETER WITH HELIUM AT 25°C AND 4.382 ATM

Flow Rate (cm^3/hr)	Δp (psid)	X (μ poise)	η (Ref. 4)	$10^{10}\ a^4/L_{eff}$ (cm^3)
120.51	0.3214	0.07	198.53	7.578
48.20	0.1288	0.03		7.588
24.10	0.0644	0.01		7.564
			Average:	7.567 $\pm$ 0.010

Table II-3 - EXPERIMENTAL VISCOSITY RESULTS FOR COMPRESSED NITROGEN AT 25°C

Pressure (atm)	Q (cm^3/hr)	η_p (μ poise)	X (μ poise)	η (this work)	η (Kestin and Leidenfrost)	Difference (%)
4.38	120.51	179.09	0.47	178.53	178.43	+ 0.06
	48.20	179.35	0.19	179.13		+ 0.39
	24.10	178.74	0.09	178.63		+ 0.11
11.19	120.51	180.98	1.21	179.56	179.34	+ 0.12
	48.20	179.96	0.48	179.29		- 0.03
	24.10	179.96	0.24	179.67		+ 0.18
21.38	120.51	184.22	2.31	181.50	180.96	+ 0.30
	48.20	182.10	0.92	181.01		+ 0.03
	24.10	182.71	0.46	182.17		+ 0.67
41.89	120.51	190.29	4.52	184.95	184.79	+ 0.09
	48.20	186.85	1.81	184.71		- 0.04
	24.10	185.77	0.91	184.70		- 0.05
69.03	120.51	200.32	7.45	191.53	191.64	- 0.06
	48.20	194.19	2.98	190.68		- 0.50
	24.10	191.90	1.49	190.15		- 0.78

Table II-4 - EXPERIMENTAL VISCOSITY RESULTS FOR LIQUID PHASE METHYL CHLORIDE AT 35 ATM

Temperature (°C)	Q (cm^3/hr)	η_p (cp)	1.18 X (cp)	η
20.00	12.051	0.1871	0.0009	0.1861
	6.026	0.1871	0.0005	0.1866
40.00	12.051	0.1577	0.0009	0.1567
	6.026	0.1565	0.0005	0.1560
60.00	24.10	0.1322	0.0019	0.1303
	12.051	0.1307	0.0009	0.1298
90.00	24.10	0.1007	0.0019	0.988
	12.051	0.0995	0.0009	0.986

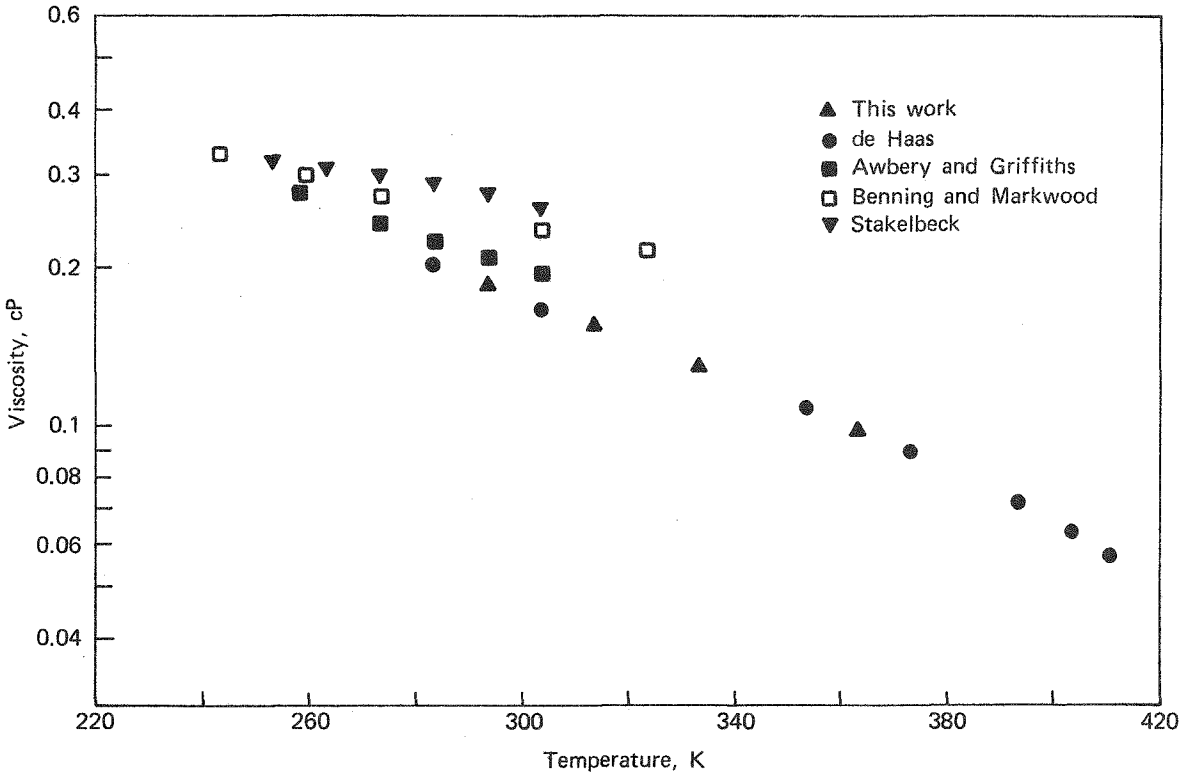

FIGURE II-3 - Viscosity of liquid phase methyl chloride.

Calcium isotope separation

W. M. Rutherford

In work previously reported [Ref. 10], we have shown that calcium isotopes can be separated by thermal diffusion of solutions of calcium compounds. A technique has been developed to offset separation of the dissolved compound from the solvent. The technique comprises setting up a controlled net flow of solvent through the thermal diffusion apparatus in a direction counter to the direction of separation of the solute from the solvent. Most of the experiments have been carried out with solutions of $Ca(NO_3)_2$ in water. Although alternative solutes and solvents have been investigated, these do not seem to offer any advantage over $Ca(NO_3)_2$.

Our immediate objective is to select optimum conditions for isotopic separation in the calcium nitrate water system. The current, as yet incomplete, series of experiments involves measurement of the separation of the ^{40}Ca-^{48}Ca pair as a function of $Ca(NO_3)_2$ concentration under both transient and steady state conditions. The results of steady state measurements indicate the ultimate separation that can be achieved in a given apparatus; whereas, the transient measurements furnish data relative to the rate at which ^{48}Ca can be produced.

We have now completed 12 experiments with counterflow in two thermal diffusion columns, one having a length of 70 cm and the second a length of 114 cm. A typical experimental setup is shown in Figure II-4. Solvent (water) is injected at a controlled

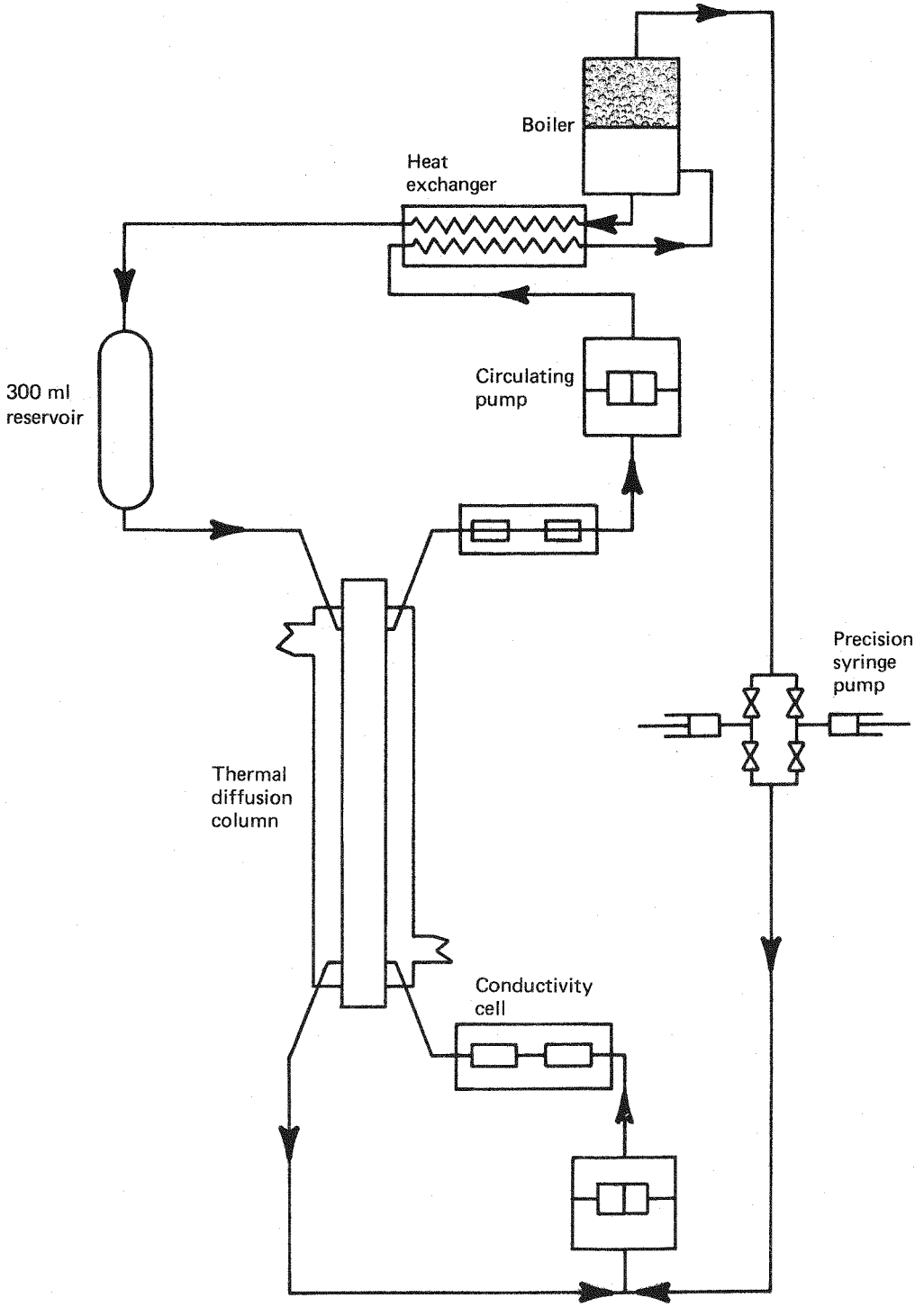

FIGURE II-5 - Solvent recycle apparatus for separation of calcium isotopes by liquid phase thermal diffusion.

rate into a circulation loop at the bottom of the column. Fluid at the top of the column is circulated through a boiler to remove solvent and through a 300-ml reservoir. The large reservoir serves to minimize changes in the chemical and isotopic composition of the fluid during the course of a run. The temperature, hence pressure, in the boiler is kept high enough to maintain single phase conditions in the column at the prevailing column operating temperatures.

Experiments have been done over a solute concentration range from about 1 to 35 percent by weight. During a typical run, which lasts several weeks, the solvent injection rate is continuously adjusted so as to maintain a concentration at the bottom of the column 2 to 3% higher than that at the top. The resulting density gradient tends to stabilize the fluid within the column against large-scale parasitic remixing of the contents.

Figure II-5 is a plot of solvent injection rate as a function of the solute concentration at the top of the column. According to theory, the required injection rate is given by:

$$\sigma = Hw_1 \qquad (1)$$

where

σ is the injection rate,

H is the initial transport coefficient for the solute-solvent pair, and

w_1 is the solvent mass fraction.

The decrease in H with concentration inferred from Equation 1 and the experimental results is due to an increase in solution viscosity at higher concentrations and probably also to a decrease in the thermal diffusion factor of the system.

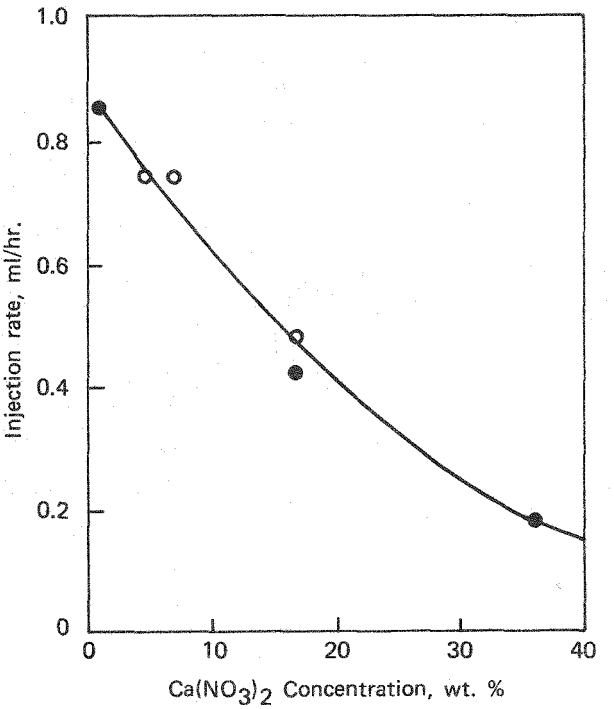

FIGURE II-5 - Solvent injection rate as a function of solute concentration for calcium isotope separation experiments. The closed circles are for the 70 cm column; the open circles are for the 114 cm column.

Isotopic ratio measurements have not been completed for all of the experiments; however, there is sufficient information at hand to get a tentative idea of the relationship between the equilibrium isotopic separation factor and solute concentration in the 70 cm column. Figure II-6 is a plot of the separation factor for the ^{40}Ca-^{48}Ca pair where the separation factor q_{48} is defined by:

$$q_{48} = \left(\frac{w_{48}}{w_{40}}\right)_B \Big/ \left(\frac{w_{48}}{w_{40}}\right)_T \qquad (2)$$

where w_{48} and w_{40} are the mass fractions of the two isotopes, and the subscripts T and B refer to the top and bottom of the column, respectively.

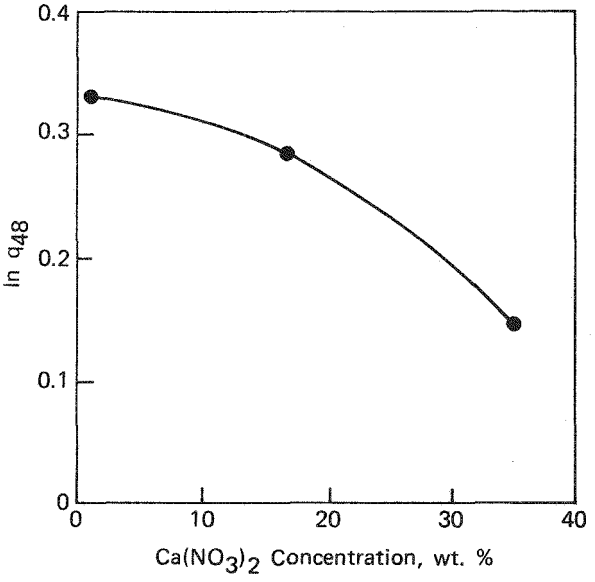

FIGURE II-6 - Equilibrium separation factor for the ^{40}Ca-^{48}Ca pair as a function of solute concentration in the 70 cm thermal diffusion column.

Figures II-7, II-8, and II-9 are plots of the $^{48}Ca/^{40}Ca$ ratio versus time for three experiments with the 70 cm column. The 300 ml reservoir had not been installed for the experiment plotted in Figure II-7; hence, there is a much larger change in the isotope ratio at the top of the column over the course of the experiment.

The quality of the transient data for the three experiments is not good enough for quantitative determination of the initial transport characteristics of the column; however, the time constants of the three runs appear to be in the range from 4 to 8 days. A new series of experiments in the longer 114 cm column is now in progress. The longer column is expected to yield larger separations, hence, better data for the transient analysis.

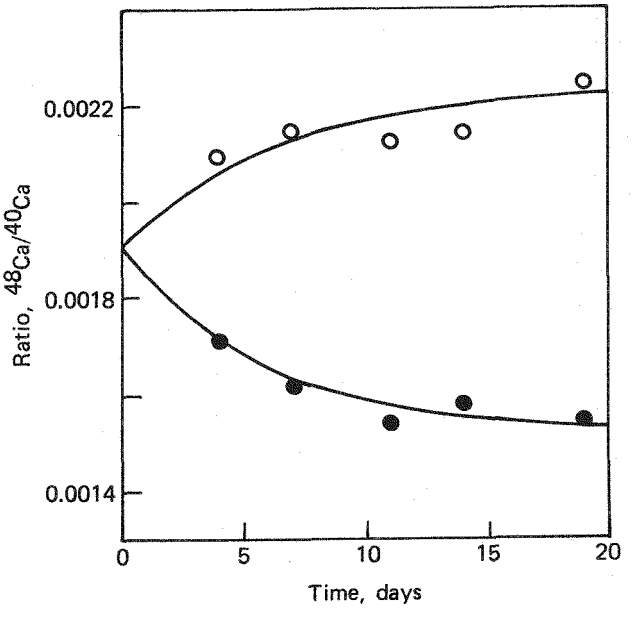

FIGURE II-7 - Separation of calcium isotopes by thermal diffusion of $Ca(NO_3)_2$ at a solute concentration of 1.3 wt %. The open circles represent samples from the bottom of the column; the filled circles, from the top.

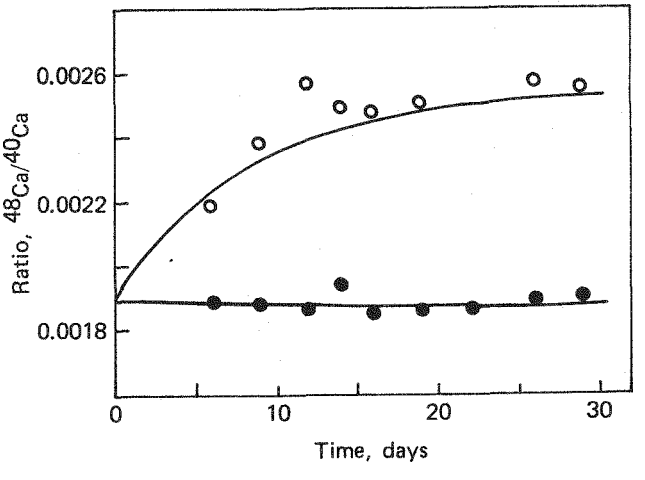

FIGURE II-8 - Separation of calcium isotopes by thermal diffusion of $Ca(NO_3)_2$ at a solute concentration of 16.7 wt %. The open circles represent samples from the bottom of the column; the filled circles, samples from the top.

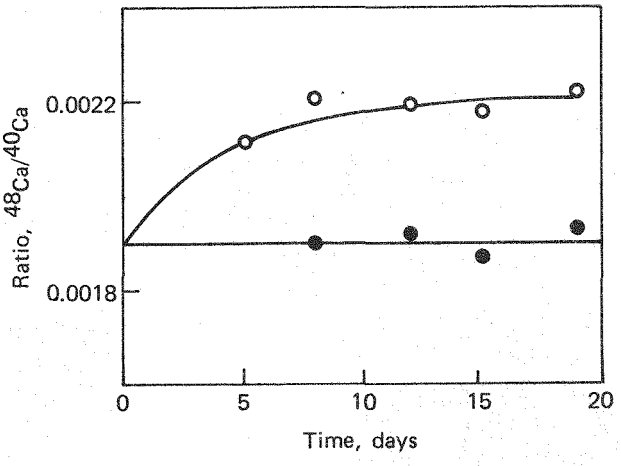

FIGURE II-9 - Separation of calcium isotopes by thermal diffusion of $Ca(NO_3)_2$ at a solute concentration of 35 wt %. The open circles represent samples from the bottom of the column; the filled circles, samples from the top.

Chemical exchange

B. E. Jepson and G. C. Shockey

The exchange of calcium ions with resin-bound cryptands has been considered as a method for enriching calcium isotopes; however, observed enrichments in column chromatography have been only modest. (See previous reports in this series.) In this report the heterogeneous exchange rate kinetics of calcium with 222B cryptand bound to Merrifield resin via an ether bond have been investigated. Merrifield resin is a low, cross-linked polystyrene polymer with 2% or less divinylbenzene; thus, it is expected to have a high porosity, generally favorable for mass transfer.

The procedure involved the equilibration of an ethanolic calcium chloride solution with 222B cryptand-resin under continuous stirring. The equilibrium fluid phase concentration at 24°C was $[Ca^{+2}] = 0.012M$ and the complexed calcium approximately 0.25 moles/g dry resin. An enriched calcium-44 solution was added to the separated fluid phase, mixed, sampled, and then remixed with the solid phase while fluid samples were withdrawn as a function of time. The isotopic compositions and fraction of exchange reaction completed are listed in Table II-5.

Table II-5 - ISOTOPIC COMPOSITIONS AND FRACTION OF EXCHANGE REACTION COMPLETED AS A FUNCTION OF TIME FOR CALCIUM EXCHANGE WITH 222B CRYPTAND

Time (hr/min)	Atom % Ca-44	Fraction Reacted (F)	ln(1-F)
0	43.4	0	0
0.5 min	36.0	0.20	-0.22
1	31.9	0.32	-0.38
2	27.1	0.45	-0.59
5	20.1	0.64	-1.02
10	12.6	0.85	-1.87
30	8.8	0.95	-3.01
1 hr	8.0	0.97	-3.59
2	7.5	0.99	-4.29
4	7.3	0.99	-4.80
8	7.1	-	-
24	7.0	-	-
31	7.1	-	-
48	7.0	-	-

Isotope exchange reactions in which no net transport of the ion occurs between the two phases are first order, and a linear relationship between time and ln(1-F) has been consistently observed for heterogeneous liquid-liquid systems. The above data, however, do not exhibit this typical response as illustrated in Figure II-10. While reaction rate limitations cannot be completely eliminated from consideration, several factors suggest that mass transfer limitations exist which result in a slow exchange rate. The non-linearity of the time ln(1-F) curve may result from the non-uniform accessibility of the anchored

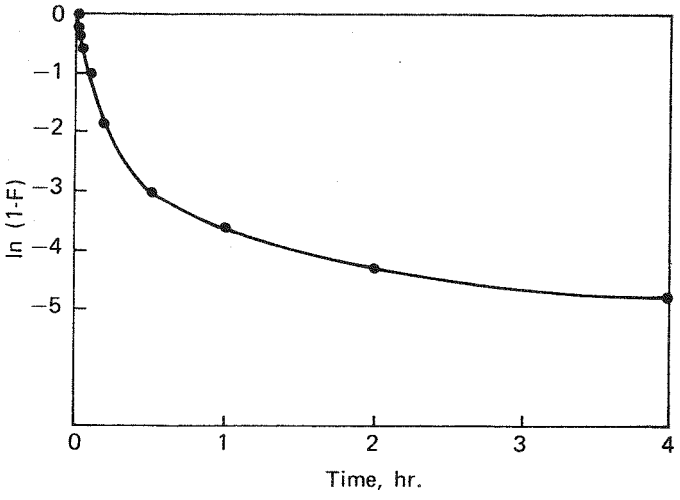

FIGURE II-10 - Exchange rate kinetics of calcium ions and 222B cryptand.

cryptand molecules to the calcium ions in solution. That is, exchange deep within the resin is expected to be limited by transport of calcium through the pores and bulk solid.

This is consistent with the relatively rapid initial exchange in which surface sites or sites near the pore openings are presumed to exchange more rapidly with the bulk fluid phase. The relatively large resin bead size, 200 to 300 μm, leads to longer pores contributing to diffusional resistance to the exchange.

A second factor is that the homogeneous exchange of calcium with 222 cryptand in water is known to be much more rapid than the above exchange. For the complexation-decomplexation reaction [Ref. 11]:

$$Ca^{+2} + 222 \text{ cryptand} \underset{k_d}{\overset{k_f}{\rightleftharpoons}} Ca(222)^{+2}$$

$$k_f = 6.6 \times 10^3 \ M^{-1}sec^{-1} \text{ and}$$

$$k_d = 0.26 \ sec^{-1}.$$

The rate limiting step for the overall homogeneous isotope exchange reaction is, then, the decomplexation step of the above reaction for which the half-time is 2.7 sec.

The requirement of rapid exchange and the subsequent shorter theoretical stage height for an isotope enrichment is quite stringent. The column packing in its currently available form cannot serve as the basis for a practical separation method; however, a reduction in bead size and an increase in porosity should show substantial improvement.

Mutual diffusion

W. L. Taylor and D. Cain

Both experimental and theoretical work on determination of the mutual diffusion coefficients of the He-, Ne-, and Xe-Ar systems have been completed. The experimental measurements were performed in the Hastelloy-X diffusion cell in the temperature range from approximately 350 to 1300 K. Final results for He-Ar were reported in Reference 12 and those for Ne-Ar were reported in Reference 13. The results for Xe-Ar are given in Table II-6. The data for all three systems are shown graphically in Figure II-11 as percent deviations from the Marrero and Mason (M&M) correlations [Ref. 14] along with other results [Ref. 15-22]. It should be noted that the recent data from Reference 17 have been added to the figures shown in References 12 and 13. Where necessary, the published data of other investigators have been adjusted to an equimolar basis according to the relation:

$$D_{12}(\chi_1=0.5) = D_{12}(\chi_1)\left[\frac{1+\Delta_{12}(\chi_1=0.5)}{1+\Delta_{12}(\chi_1)}\right]$$

Table II-6 - DIFFUSION COEFFICIENTS OF XENON-ARGON AT ONE ATMOSPHERE PRESSURE, EQUIMOLAR EQUILIBRIUM CONCENTRATION

Temperature (K)	D_{12} (cm^2/sec)
344	0.146
431	0.232
500	0.291
513	0.294
571	0.387
592	0.405
656	0.471
732	0.592
767	0.648
822	0.717
890	0.820
948	0.908
1013	1.050
1106	1.159
1137	1.232
1244	1.470
1256	1.493

$D_{12}(X_1)$ is the value of diffusion coefficient measured at mole fraction X_1 and the Δ_{12}'s are calculated from Equation 4.2-1 of Reference 14 with the constants given in their Table 15. The dot-dash curves (·-) in Figure II-11 represent the present data fitted to a M&M type function by the method of least squares.

Marrero and Mason [Ref. 14] have fitted many binary diffusion coefficients to a correlating function (denoted here "M&M") of the form:

$$\ell n(pD_{12}) = \ell nA + s\ \ell nT - \ell n[\ell n(\phi_o/kT)]^2 - S/T - S'T^2$$

where A, s, ϕ_o, S and S' are empirical constants and k is Boltzmann's constant. The term containing ϕ_o is related to the high energy portion of the intermolecular potential which is generally assumed to be an exponential repulsion. The transport collision integral for diffusion, $\Omega_{12}^{(1,1)*}$, is then approximately proportional to $[\ell n(\phi_o/kT)]^2$ at high temperature. The value of ϕ_o is usually inferred from high energy interactions such as *ab initio* calculations or molecular beam scattering cross sections. The parameter s represents the primary temperature dependence of D_{12} and should be approximately 3/2. The parameters S and S' are related to the attractive portion of the intermolecular potential, but we consider them, along with A, to be adjustable. We used the M&M correlating function with the parameters given by Marrero and Mason as our starting point; e.g., we compare our measurements, along with other experimental diffusion data not contained in the correlations, to the aggregate of previous results, as represented by the M&M correlations. The ϕ_o term in the correlating function is taken from Reference 14 with other parameters being determined from the data.

The available high temperature data include three sets: a) the present work, b) Hogervorst [Ref. 16], and c) Zwakhals and Reus [Ref. 17]. For He-Ar and Ne-Ar, the data of Zwakhals and Reus lie between our data and Hogervorst's, but within our mutual uncertainty and that of the M&M correlation. For Xe-Ar, the Zwakhals and Reus data fall considerably below our data, Hogervorst's, and the lower uncertainty bound of the M&M correlation.

Unfortunately, the data in Reference 17 suffer extreme deviations around room temperature, where the M&M correlation is most reliable, leading one to distrust the overall reliability in their work. The very precise data of Arora, et al. [Ref. 15] at 300 K should be noted here, in that they corroborate the validity of the M&M correlations at room temperature for all three systems. Furthermore, these authors were

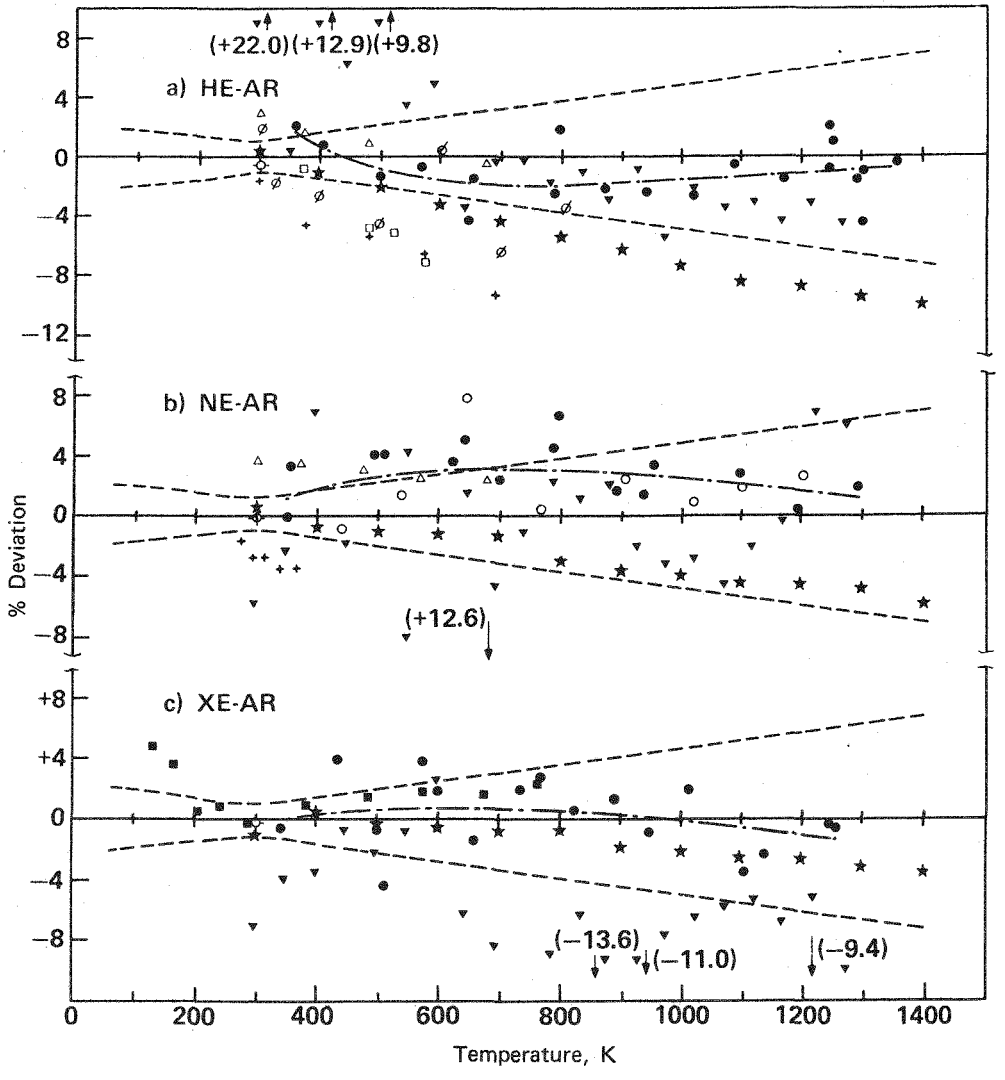

FIGURE II-11 - Percent deviation of experimental diffusion coefficients from the Marrero and Mason correlation functions. The experimental points are those measured subsequently to and not included in the correlations. They are: (a) HE-AR ●, present data; *, Hogervorst [Ref. 16]; ▼, Zwakhals and Reus [Ref. 17]; △, Kalinen and Suetin [Ref. 18]; □, Suetin, et al, glass capillary, and +, metal capillary [Ref. 19]; Ø, Liner and Weissman [Ref. 20]; and ⊹, Arora, et al. [Ref. 15]. The curves are: Abscissa (or baseline), Marrero and Mason correlation function with ±---, the reported uncertainty in the correlation [Ref. 14]; _·, least square fit to the present data. (b) NE-AR same as above except that ● represents natural isotopic abundance neon; ○ represents neon-22; and +, Nain and Saxena [Ref. 21]. (c) XE-AR same as above except ■, Loiko, et al. [Ref. 22].

not able to reproduce Hogervorst's data above 700 K by an extrapolation based on their data and on an intermolecular potential derived therefrom. Finally, the He-Ar interaction has been studied in detail by Aziz, et al. [Ref. 23] who found it impossible to reproduce the Hogervorst data using potentials based on their differential scattering cross sections. It would appear that the M&M correlations provide a fairly reliable value for D_{12} for these three systems, even when extrapolated to high temperatures.

We have also used other recent transport property data to test the consistency of the diffusion measurements. Mutual consistency relations are obtained by expressing one transport property as a function of one or more other measured properties via combinations of the transport collision integrals, or as temperature derivatives of functionals of these properties. The final result is an expression which is either completely independent of knowledge of the molecular interactions, or which introduces the force law in the least sensitive manner possible. The consistency relations used here involve: a) using accurate viscosity data to calculate diffusion coefficients, and b) using the temperature dependence of the thermal diffusion factor to obtain the logarithmic temperature derivative of the diffusion coefficient, then fitting this point by point to the M&M correlation function.

The theoretical details for the viscosity/mutual diffusion relations are given in Reference 24 while the details for the thermal diffusion/mutual diffusion relation are given in Reference 13. A comparison of transport properties for all three systems was made. These results, along with percent deviations of $[D_{12}]$ values computed from available intermolecular potentials for the unlike interactions, are shown in Figure II-12. The baseline is the diffusion coefficient as calculated from the thermal diffusion correlations given by Taylor [Ref. 25] which were derived from all available thermal diffusion factors for each of the three systems. This property was chosen as the baseline because α_T provides a sensitive test of the unlike interaction. Furthermore, at the time the M&M correlations were derived, experimental diffusion data were available only from ∿500 to 600 K. Thermal diffusion probes the repulsive wall of the potential at higher reduced temperatures than ordinary diffusion [Ref. 26], so α_T correlations based on data up to ∿900 K would be consistent with recent D_{12} data at even higher temperatures. The parameters derived by the method outlined are given in Reference 13. Diffusion coefficients from mixture viscosities were calculated as outlined in Reference 24. Percent deviation as represented by

$$\% \text{ Dev} = \left([D_{12}]_\eta - [D_{12}]_{\alpha_T}\right)/[D_{12}]_{\alpha_T} \times 100$$

is shown in Figure II-12 by the heavy dotted lines. The experimentally measured diffusion coefficients were fitted by least squares to the M&M function, and the average root-mean-square (r.m.s.) deviation of the points was evaluated. The shaded area represents the percent deviation obtained above with $[D_{12}]_\eta$ replaced by $[D_{12}]_{exp}$. The band width of the shaded area is the ±r.m.s. deviation of the points. The various other curves represent percent deviations of theoretical diffusion coefficients, $[D_{12}]_{Th}$, computed in the second approximation from intermolecular potentials proposed in the literature; e.g., $[D_{12}]_\eta$ is replaced by $[D_{12}]_{Th}$. The solid curves are the original M&M correlations.

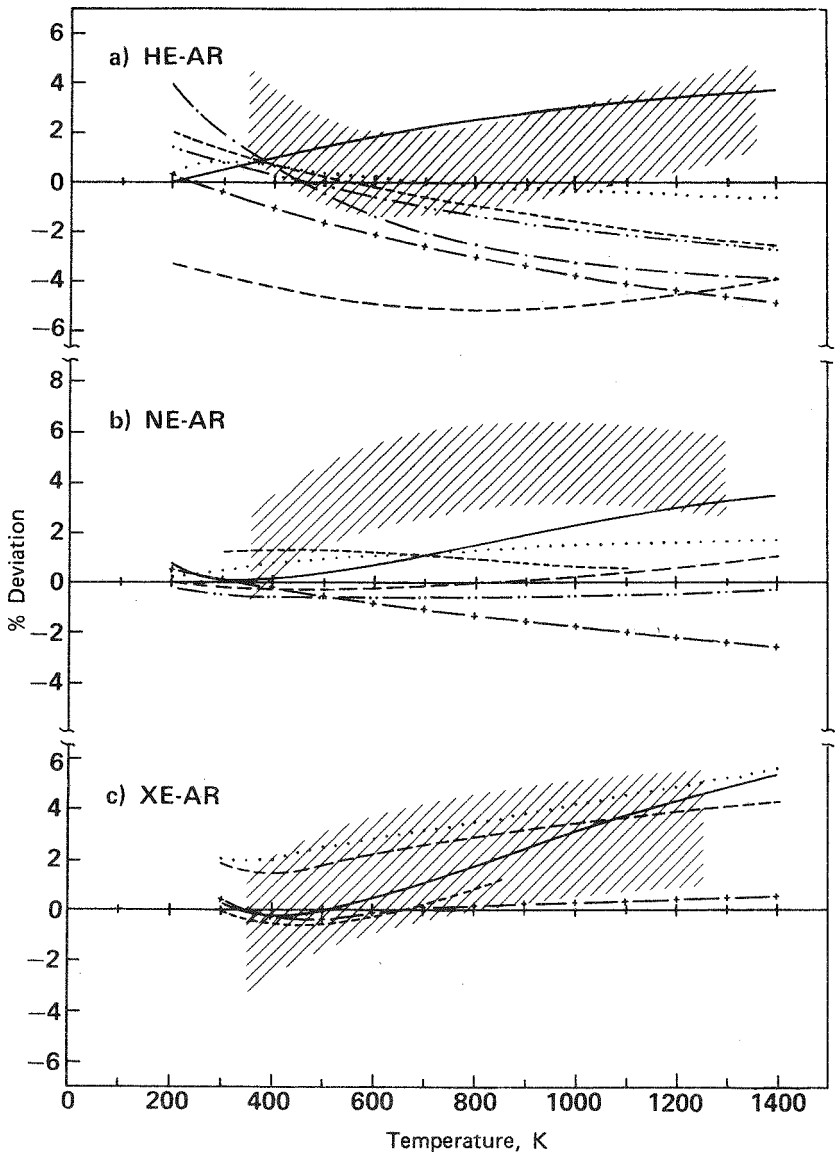

FIGURE II-12 - Mutual consistency of the present diffusion data with thermal diffusion, viscosity, and previous diffusion data along with the theoretical predictions of several intermolecular potentials for each of the binary X-AR systems. The baselines represent diffusion coefficients calculated from thermal diffusion correlations [Ref. 25] by the method given in [Ref. 13] and the curves represent percent deviations from these "standards." The experimentally derived curves are: shaded area, the present data fitted to an M&M-type function by the method of least squares with the band-width twice the r.m.s. deviation of the points; —, the M&M correlation [Ref. 14]; and ''''', obtained from viscosity data as explained in text. The theoretical curves are: ---, Dymond-Alder potential [Ref. 26] with parameters by Lin and Robinson [Ref. 27]; —·, ESMSV potential [Ref. 28]; —+, (M-6-8) potential [Ref. 15]; ····, Exp-6 potential [Ref. 29]; and —· ·, HFD potential with parameters by Aziz, et al. [Ref. 23] for HE-AR and Ahlrichs, et al. [Ref. 30] for NE-AR.

He-Ar

Five intermolecular potentials were used to calculate diffusion coefficients. The potentials shown are those proposed in the literature which have been specifically fitted to helium-argon data other than the diffusion data of Hogervorst. Lin and Robinson [Ref. 27] have determined parameters for the reduced Dymond-Alder (DA) [Ref. 26] potential from interaction second virial coefficients of mixtures of helium and argon; Chen, et al. [Ref. 28] have fitted the Exponential-Spline-Morse-Spline-Van der Waals (ESMSV) form to low energy differential cross sections and second virial coefficients; the parameters for the Hartree-Fock-Dispersion (HFD) were obtained by Aziz, et al. [Ref. 23] from differential cross sections; and Arora, et al. [Ref. 15] provided parameters for the (M-6-8) potential from their diffusion data. These four potentials all predict D_{12} values which are low compared to experimental diffusion coefficients, as well as viscosity and thermal diffusion. The trend is particularly imprecise at high temperatures. The fifth potential, the exponential-6 (exp-6) of Mason and Rice [Ref. 29] does a very adequate job of representing the experimental properties over the entire temperature range. On the basis of Figure II-12, it would appear that diffusion, viscosity, and thermal diffusion are mutually consistent within ∿6% up to 1400 K, with the (exp-6) potential predicting theoretical values most accurately.

Ne-Ar

The theoretical potentials are the same as in Figure II-12 except that the HFD parameters were obtained by Ahlrichs, et al. [Ref. 30] from *ab initio* and semi-empirical calculations. Despite the fact that the present Ne (natural abundance)/Ar, ^{22}Ne/Ar, and the Kalinen and Suetin [Ref. 18] data are all consistent, they fall well above the baseline, as well as the $[D_{12}]_\eta$ curve and the predicted $[D_{12}]_{Th}$ which are all mutually consistent with $[D_{12}]_\eta$ and the baseline to ∿6%.

Xe-Ar

The mutual consistency is slightly more satisfactory for this system with the M&M correlation rising to ∿5% above the baseline. The present data and $[D_{12}]_\eta$ follow the baseline more closely and are best represented by the (M-6-8) potential. Overall mutual consistency of the transport properties in the temperature range is about 5%.

We conclude that the present measurements of He-, Ne-, and Xe-Ar taken in a temperature range extending over ∿1000 K agree, within the stated uncertainty, with the Marrero amd Mason correlations [Ref. 14] derived from diffusion and molecular beam cross section data. Diffusion coefficients derived from thermal diffusion factors are, in all cases, lower than the M&M correlations but within the lower error bound. Viscosity-derived diffusion coefficients for Ne-Ar and Xe-Ar were mutually consistent with the other properties, but $[D_{12}]_\eta$ for He-Ar appears to be too low at high temperatures. The data of Hogervorst also appear to be too low for He-Ar at high temperatures, falling slightly below $[D_{12}]_\eta$. Our data tend to be too high for Ne-Ar with respect to thermal diffusion and viscosity, but lie within the upper error bound of the M&M correlation. Therefore, despite some inconsistencies, the transport properties are mutually consistent to within

∿5 to 6% at the worst at the highest temperatures and probably better than ∿2 to 3% in the lower half of the temperature range. A specific intermolecular potential can be chosen for each system. Until the properties are brought into still closer agreement, however, it is difficult to choose a preferred form of the potential.

Molecular beam scattering

R. W. York and W. L. Taylor

HARDWARE DEVELOPMENT

The triple-pumped detector system has undergone final internal helium leak testing including a LN_2 cold shock test. All tests were completed satisfactorily, and cold shrinkage centerline position measurements were made for the entrance orifices with respect to the ion region center. The detector was partially assembled for vacuum tests while mounted on its chamber mounting flange with rotary bearing and vacuum seals.

Both 90° arms of the beam chamber were aligned with a laser using a new precision mounting system of in-house design. This system enabled the laser to be passed through all of the beam-forming components in one arm, then reflected by a prism that was accurately positioned at the final center of rotation of the new detector. The reflected laser beam was then allowed to pass through all of the beam-forming components of the second chamber arm and all component adjustments were optimized for maximum laser beam intensity. Due to the limitations of these adjustments, the detector mounting height had to be raised by 0.125 in. to permit the vertical position to the detector entrance orifice to accurately coincide with the beam axis. A new sealing retainer ring was fabricated to accomplish this height change.

The detector system was then successfully installed on the beam chamber with its ionizer and three 60-liters/sec ion pumps mounted. The servo-rotation drive assembly for the detector was installed with an angular position indicator and chamber hangers were modified for adequate clearance during the required detector rotation. Due to the added weight of the new system and the necessary retensioning of the main chamber hanger supports, a complete realignment of all beam components was required. This was accomplished with the laser system and prism mounted directly on the detector with its reflecting surface accurately located at the collision zone center. Readjustment of the beam forming components was made to enable the laser beam to again successfully pass through the primary beam chamber arm and reflect out through the secondary beam arm for maximum beam intensity.

The chamber has been closed for initial vacuum tests on the detector rotary seal and outgassing. The quadrupole housing portion of the detector is currently being modified for fit. The quadrupole will be assembled in the housing with all final internal wiring and installed as an integral unit on the detector after initial rotary vacuum seal operation has been tested satisfactorily.

The bell jar test system containing the velocity selector has been modified to include a differentially-pumped detector assembly. This will produce an improvement in the signal to noise ratio of approximately two orders of magnitude over previous efforts. This new system has been

fabricated, completely installed, and helium leak tested. The system has been evacuated to the 10^{-8} torr range and is nearly ready for selector evaluation tests.

TOTAL CROSS SECTIONS

Molecular beam scattering experiments have for many years been a useful tool in the investigation of interatomic forces. Two general types of scattering experiments can be conducted in the laboratory on non-reactive particles:
a) attenuation of a beam passing through a scattering gas of varying density, or
b) determination of the intensity of particles scattered from a collision zone as a function of angle at constant relative energy. In principle, if experiment (a) is conducted for all possible energies, or if (b) is measured over all angles, sufficient information is contained in either of these experiments to specify the interaction energy of the collision as a function of distance; e.g., the interatomic potential. In practice, the ideal experiment is yet to be achieved because of such things as beam intensity/detector sensitivity, angular resolution, and velocity distributions in the scattered and scattering particles. These practical aspects of limitations of an experiment tend to blur the precision with which the microscopic two-particle interaction can be determined. In particular, the detector sensitivity, as expressed by the signal/(background) noise ratio must be several orders of magnitude better for experiment (b) as compared to experiment (a). The hardware development described above is intended to improve our signal/noise ratio so that measurements can be made off the beam axis as a function of angle; e.g., the measurement of differential cross sections.

We have previously published total cross section results for the Ar-Kr [Ref. 31] and Ne-Ar [Ref. 32] systems. Recently, we measured and reported [Ref. 33] total cross sections for the He-Ar system in the velocity range from approximately 8 to 20 x 10^4 cm/sec. These data showed good reproducibility and precision. Absolute values for the cross sections were within approximately 5% of another recent set of measurements [Ref. 34]. The present data are therefore considered reliable enough to serve as a coarse filter for the He-Ar interatomic potential. A literature search identified seven published potentials for this system. Values for the force constants for the potentials are given in Table II-7. Theoretical total cross sections were computed for each of these potentials using the WKB (Wentzel-Kramers-Brillouin) approximation for the scattering phase shifts, η_ℓ, which were then summed to obtain the cross sections. A test case in which the Schroedinger wave equation was solved by direct numerical integration verified the WKB method accurate to about 1% in the velocity range covered by the experiments. The experimental cross sections were then smoothed by fitting to a representative mathematical function by the method of least squares. Percent deviations are represented by:

$$\% \text{ Dev} = (Q_{Th} - Q_{Exp})/Q_{Exp} \times 100$$

were then calculated in each case as a function of relative velocity, and the results are shown in Figure II-13. The results do appear to act as a reasonable filter for the potentials. The best fit is the DA potential while, on the other hand, it is obvious that the (m-6-8) is realistic only around 18 to 20 x 10^4 cm/sec, approximately equivalent to the room temperature data. This is logical, as the (m-6-8) parameters were derived from accurate room temperature diffusion data.

Table II-7 - FORCE PARAMETERS FOR He-Ar INTERATOMIC POTENTIALS

Potential	ε/h (K)	r_m (Å)	Source
Dymond-Alder (DA)	31.12	3.051	Ref. 35,36
Exponential-6 (Exp-6)	33.59	3.500	Ref. 37
Exponential-Spline-Morse-Spline-Van der Waals (ESMSV)	24.20	3.540	Ref. 38
Hartree-Fock-Debye (HFD)	29.80	3.480	Ref. 39
Inverse Power (m-6-8)	22.50	3.661	Ref. 40
Maitland-Smith (MS)	30.00	3.434	Ref. 41
Morse-Morse-Spline-Van der Waals (M2SV)	20.89	3.659	Ref. 42

Also, allowing for the possibility that our data are somewhat high (we are approximately 5% above Pirani and Vecchiocattivi), then the HFD or MS potentials would be the next choices. The Exp-6 predicts cross sections that are much too high at low relative velocities but is fairly close around the equivalent of room temperature. The ESMSV is far too low over the entire range. Further testing of DA and HFD or MS against other microscopic properties in the temperature range 77 to 375 K will be desirable.

Calcium isotope enrichment

E. Michaels

EQUIPMENT DESCRIPTION

An experimental liquid-liquid extraction system was constructed to evaluate the calcium chemical exchange system's hydrodynamic behavior in reciprocating plate columns. A schematic drawing of the system is shown in Figure II-14. The contractor is a Karr reciprocating plate extraction column 2 in. in diameter. This type of contactor is characterized by plates that have a large free area (58.8%). The plates are made of Teflon and connected to a central Hastelloy shaft which is driven by a 1/4 hp motor. The column is made of borosilicate glass flanged together with Teflon-filled TMEG gaskets. At the top of the contacting section of the column is a custom-made stainless steel 316 disengaging chamber; the large volume of this chamber was necessary to allow for gravity separation of the two phases.

The 1.3 M $Ca(TFA)_2$ aqueous solution (ρ = 1.15 g/cm^3) and 0.7 M $Ca(TFA)_2$·crown organic solution (ρ = 1.4 g/cm^3) were fed countercurrently to the column. The feed pumps are pulsafeeder #7120 metering pumps; the feed flows are manually set and remain constant throughout an experimental run. Flowmeters in the feed lines allow the flows to be monitored. Each phase is pumped out of the contactor by automatically controlled Pulsafeeder #7120-AP pumps. For the aqueous phase, a Princo level probe in the disengaging chamber sends a signal to the Fisher TL109, PID controller. The controller then sends a signal to the automatic pump to increase or decrease its capacity. This system has been successful in maintaining the desired level set point. For the organic phase, a Drexelbrook interface probe sends a signal to the controller,

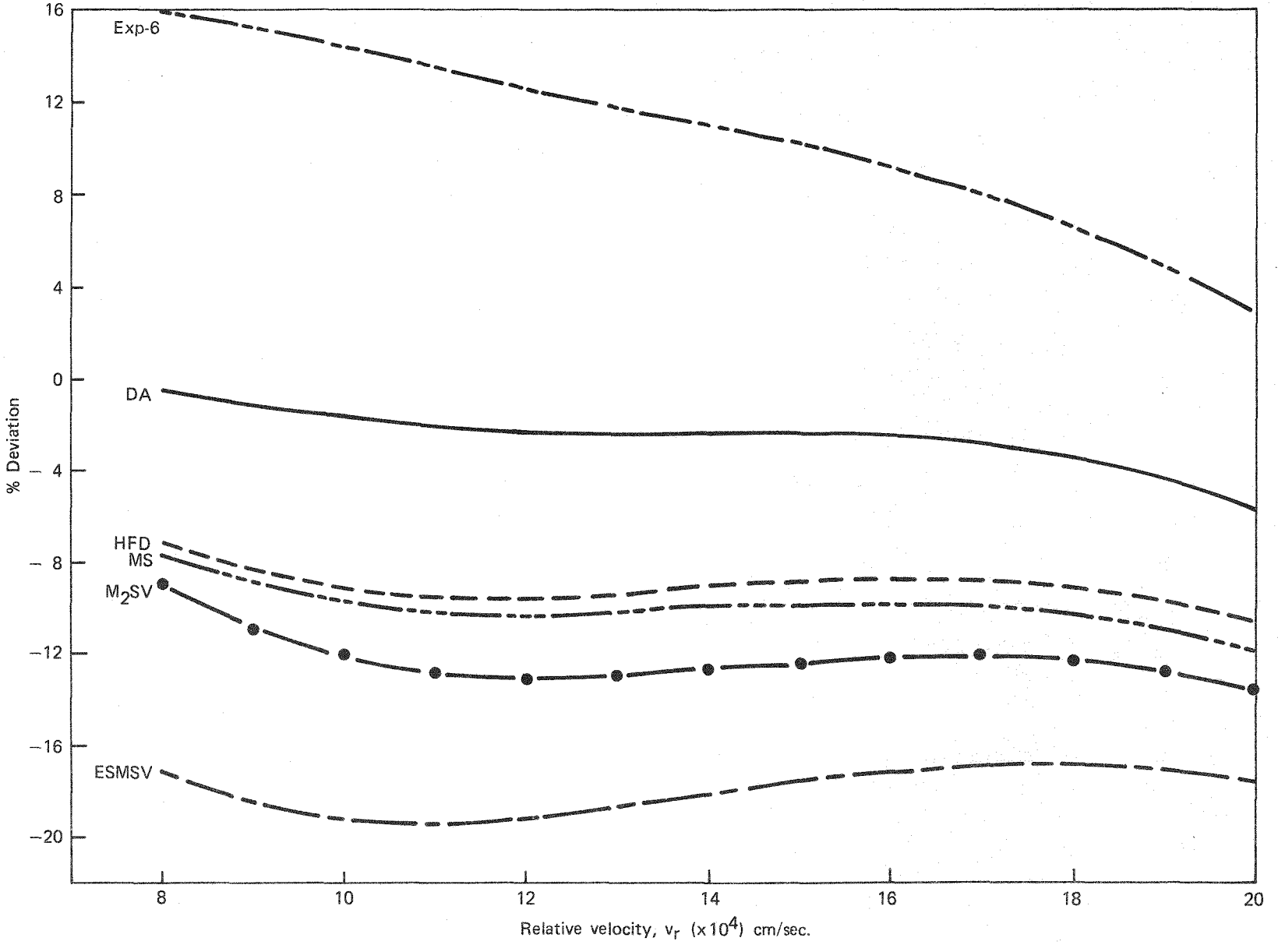

FIGURE II-13 - Percent deviations of theoretical interactomic potentials for He-Ar from the smoothed experimental results. The curves are: —, DA [Ref. 35,36]; - - -, Exp-6 [Ref. 37]; -—, ESMSV [Ref. 38]; --- HFD [Ref. 39]; ·····, (m-6-8) [Ref. 40]; -·-·-, MS [Ref. 41]; and +—, M2SV [Ref. 42].

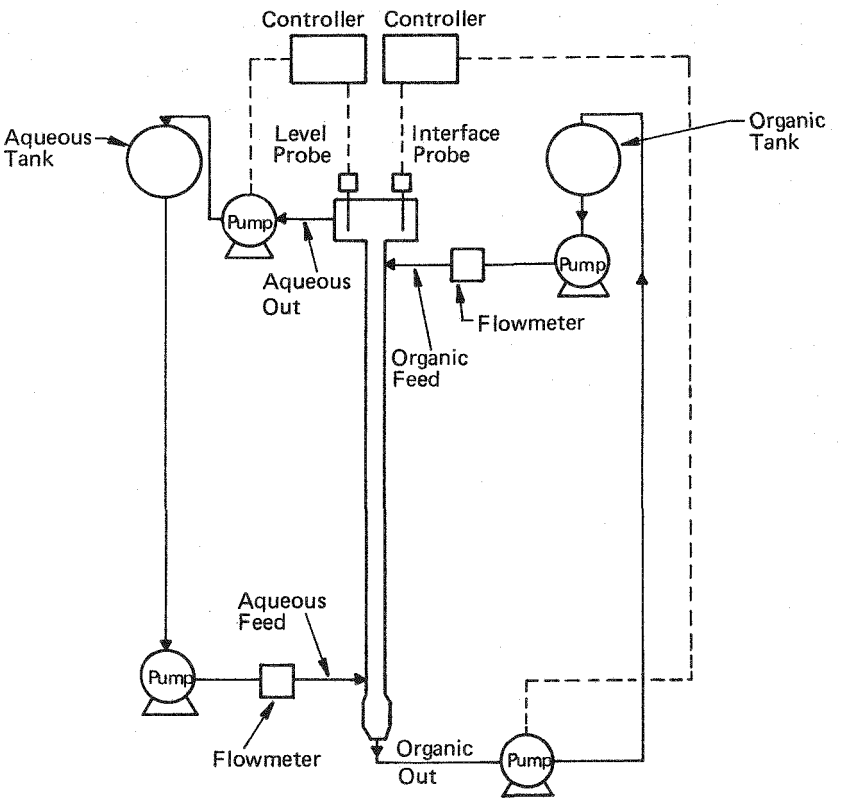

FIGURE II-14 - Schematic of Karr Column Test Facility.

and the controller then regulates the organic pump. In these experiments, the interface probe had not been able to accurately detect the level so the interface was controlled by manually adjusting the controller output.

EXPERIMENTAL

To characterize the hydrodynamics of the calcium chemical exchange system in a Karr column, three variables need to be looked at: the amplitude of the reciprocating stroke, A; the superficial velocities of each phase U_c, U_d; and the stroke frequency. It has been found that the minimum HTU in a Karr column occurs close to the flooding point [Ref. 43]. As a result, the models and correlations developed for this equipment require information obtained at or near flooding.

The purpose of this study was to obtain data for A, F, U_c, and U_d at flooding and to see whether the calcium chemical exchange system fits the models developed.

Two types of experiments were performed. Experiments 1A, 2, 3, 4, and 5 were done with five different flow rates. During these experiments, the flow rate and stroke amplitude were held constant, and the stroke frequency was increased incrementally until the frequency needed to flood the column was determined. In experiments 1A, 1B, and 1C the flow rates were all the same, the stroke amplitude was varied, and the flooding frequency determined.

Because of the constraint of equimolar flow in an isotope exchange process, the $\left(\frac{U_d}{U_c}\right)$ ratio is always constant.

There are two types of flooding that can occur in a Karr column [Ref. 44]. The first is emulsion flooding where, due to the agitation, the two phases form an emulsion and cannot coalesce. The second type is entrainment flooding, where small drops of the dispersed phase are swept down the column by the continuous phase. A prediction of the type of flooding to occur can be made by evaluating ε_f, the holdup at flooding. If ε_f is between 0.33 and 0.5, emulsion flooding occurs; if ε_f is less than 0.33, then entrainment flooding occurs. ε_f is calculated from the equation [Ref. 45]:

$$\varepsilon_f = \frac{(L^2 + 8L)^{0.5} - 3L}{4(1 - L)} \qquad (1)$$

where $L = \frac{U_d}{U_c} = 0.54$ for our system.

This gives $\varepsilon = 0.29$ and means that we should see entrainment.

RESULTS

Observations revealed entrainment of very small drops of aqueous phase in the continuous phase, and the collection of the drops in the expanded section just below the aqueous feed. This confirmed the prediction of entrainment flooding. Initially, we believed that the entrainment of the drops was not flooding until actual coalescence took place forming an interface at the bottom. After we evaluated the data, it was apparent that for the higher flow rates, where the higher viscosity continuous phase was moving relatively quickly down the column, entrainment flooding had occurred at frequencies about 15% lower than those recorded during the experiments. Also, it was determined that the system equilibrates to any adjustments in approximately 15 min.

The correlation developed [Ref. 44] for the flooding velocity with a circulating drop is:

$$U_{sf} = 0.01851 \frac{(1 - \varepsilon_f)^2}{\varepsilon_f^{1/3}} \left[\frac{\gamma^3 \sigma^4 h^2}{\rho^{-3} (Af)^6 (1-\sigma^2)^2}\right]^{0.2} \left[\frac{g^2 \Delta\rho^2}{\mu c \rho c}\right]^{1/3} \qquad (2)$$

It should be noted that we are using the circulating drop assumption rather than the rigid drop because our continuous phase is the organic phase, which is considerably more viscous than the dispersed aqueous phase and, in this case, drop circulation is encouraged [Ref. 44].

To test this correlation, a plot of U_s observed vs. U_s calculated was made. The correlation is represented by the 45° line drawn on Figure II-15. U_s OBS was found by using the known superficial velocities for each phase in Equation 3. The equation [Ref. 44] $U_{sf} = U_{df} \frac{(1-\varepsilon_f)}{\varepsilon_f} + U_{cf}$.

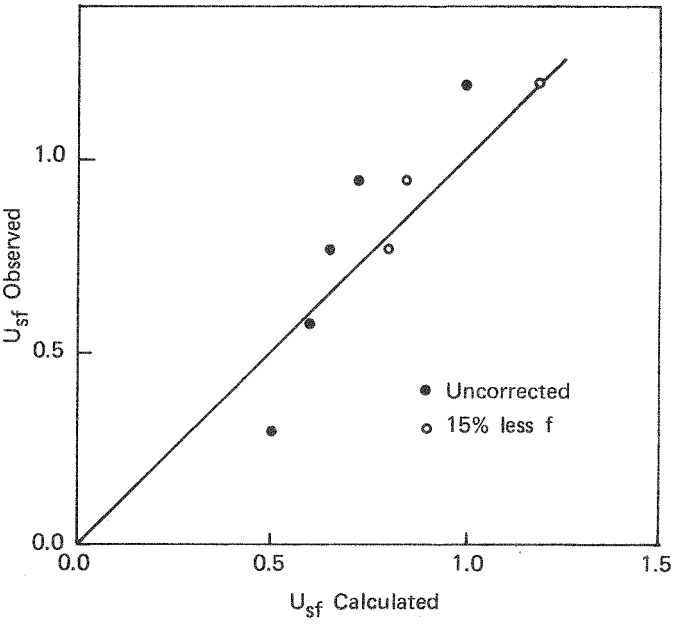

FIGURE II-15 - Comparison of observed and calculated slip velocities at flooding.

The calculated values of U_{sf} OBS and U_{sf} CALC appear in Table II-8. As can be seen, the experimental values are offset from the curve at the higher flow rates. If U_{sf} is recalculated using frequencies 15% lower, one can see that the agreement with the correlation is much better.

Another method of checking the flooding data and correlation is to take the U_{sf} CALC and back calculate U_d and U_c. U_c can then be used along with Q_c to calculate the flooding diameter of the column by the equation [Ref. 46]:

$$D_f = \frac{(4\ Q_c)^{1/2}}{\pi\ U_c} \quad .$$

In the case of the three higher flow experiments, the calculated diameter was 8-15% larger than the actual column (5.08 cm). When the diameters were calculated with a 15% lower frequency, the error in the diameter was 0-5% (see Table II-8).

As a result of our experimental findings, we concluded that the circulating drop correlation does a good job in characterizing the calcium isotope chemical system.

The next step in evaluating the Karr column performance is to extend the correlation from the flooding point to the operating point. Karr and others have found the minimum HETS just below the flooding point [Ref. 43], so all further calculations will be based on operating the column at 80% of the correlation flooding frequency. These results are tabulated in Table II-9.

The first calculation is done by setting Equation 2 and Equation 3 equal to each other, inserting the known U_d, U_c, and physical property data, and solving for each frequency [Ref. 46]. Next, the drop diameter is found via Equation 4 and 5 [Ref. 47,48].

$$\psi = (2/3)\pi^{2-\rho} \frac{1 - \sigma^2}{h\ Co^2\sigma^2}(Af)^3 \qquad (4)$$

$$d_{32} = 0.36\left[\frac{\gamma^3}{\psi^{2-\rho}}\right]^{0.2} \qquad (5)$$

Once ε and d_{32} are known, the specific interfacial area is calculated:

$$a = \frac{6\varepsilon}{d_{32}} \qquad (6)$$

The overall mass transfer coefficient can be calculated based on the individual film coefficients.

$$K_c = \left[\frac{1}{k_c} + \frac{1}{mk_d}\right]^{-1} \qquad (7)$$

Estimation of the individual film coefficients for circulating drops can be made as reported by Ladda as follows [Ref. 49]:

$$Sh = \frac{k_c\ d_{32}}{D} \qquad (8)$$

$$Sh = 1.13\ (Pe)^{1/2}$$

$$Pe = Re\ Sc$$

$$= d_{32}\ \frac{v_{t\rho}}{\mu}\ \frac{\mu}{\rho D} \qquad (10)$$

$$Pe = \frac{d_{32}\ v_t}{D}$$

v_t, the terminal drop velocity, is determined from a correlation in Treybal [Ref. 50] for μ_c not exceeding 30 cp.

Also from Ladda:

$$k_d = 0.00375\ v_t\left(\frac{\mu_c}{\mu_c + \mu_d}\right) \qquad (11)$$

M is the isotopic distribution ratio for the chemical exchange process and has been found to be 1.008 [Ref. 51].

With K_c calculated, the height of a transfer unit can be calculated.

Table II-8 - OBSERVED FLOODING VELOCITIES FOR KARR COLUMN EXPERIMENTS

	1A		1B		1C	
	$Q_c = 10.67 \frac{cm^3}{sec}$ $U_c = 0.53 \frac{cm}{sec}$	$Q_d = 5.73$ $U_d = 0.28$	$Q_c = 10.67$ $U_c = 0.53$	$Q_d = 5.73$ $U_d = 0.28$	$Q_c = 10.67$ $U_c = 0.53$	$Q_d = 5.73$ $U_d = 0.28$
	Experimental Data	15% Lower Frequency	Experimental Data	15% Lower Frequency	Experimental Data	15% Lower Frequency
A	2.54 cm	2.54	1.91	1.91	1.27	1.27
f	1.33 sec^{-1}	1.13	1.93	1.64	2.8	2.38
ψ	346 erg/cm^3 sec		449		404	
d_{32}	0.13 cm		0.118		0.123	
U_s OBS	1.2 cm/sec	1.2	1.2	1.2	1.2	1.2
U_s CALC	0.98 cm/sec	1.19	0.89	1.07	0.92	1.12
U_c	0.42 cm/sec	0.51	0.38	0.46	0.40	0.48
U_d	0.23 cm/sec	0.28	0.21	0.25	0.21	0.26
D_f	5.69 cm	5.16	5.98	5.06	5.83	5.32

	2		3		4	5
	$Q_c = 8.33$ $U_c = 0.41$	$Q_d = 4.47$ $U_d = 6.22$	$Q_c = 6.67$ $U_c = 0.33$	$Q_d = 3.58$ $U_d = 0.18$	$Q_c = 5.0$ $Q_d = 2.68$ $U_c = 0.25$ $U_d = 0.13$	$Q_c = 2.5$ $Q_d = 1.3$ $U_c = 0.12$ $U_d = 0.07$
	Experimental Data	15% Lower Frequency	Experimental Data	15% Lower Frequency	Experimental Data	Experimental Data
A	2.54	2.54	2.54	2.54	2.54	2.54
f	1.73	1.5	1.86	1.58	2.0	2.33
ψ	767		958		1178	1871
d_{32}	0.095		0.087		0.080	0.067
U_s OBS	0.95	0.95	0.77	0.77	0.57	0.29
U_s CALC	0.72	0.85	0.65	0.80	0.60	0.50
U_c	0.31	0.37	0.28	0.34	0.26	0.22
U_d	0.17	0.20	0.15	0.19	0.14	0.12
D_f	5.85	5.35	5.51	5.0	4.95	3.80

Table II-9 - SUMMARY OF MEASURED FLOODING VELOCITIES AND ESTIMATED RESIDENCE TIMES FOR KARR COLUMNS

80% Below Correlation

1A	1B	1C	2	3	4	5
Q_c = 10.67 cm^3/sec	Q_c = 10.67	Q_c = 10.67	Q_c = 8.33	Q_c = 6.67	Q_c = 5.0	Q_c = 2.5
U_c = 0.53 cm/sec	U_c = 0.53	U_c = 0.53	U_c = 0.41	U_c = 0.33	Q_c = 0.25	U_c = 0.12
Q_d = 5.73 cm^3/sec	Q_d = 5.73	Q_d = 5.73	Q_d = 4.47	Q_d = 3.58	Q_d = 2.68	Q_d = 1.3
U_d = 0.28 cm/sec	U_d = 0.28	U_d = 0.28	U_d = 0.22	U_d = 0.18	U_d = 0.13	U_d = 0.07
A = 2.54 cm	A = 1.91	A = 1.27	A = 2.54	A = 2.54	A = 2.54	A = 2.54
f = 55.91 sec^{-1}	f = 1.31	f = 1.90	f = 1.20	f = 1.27	f = 1.6	f = 2.72
$\varepsilon=\phi$ = 0.42	$\varepsilon=\phi$ = 0.38	$\varepsilon=\phi$ = 0.40	$\varepsilon=\phi$ = 0.38	$\varepsilon=\phi$ = 0.44	$\varepsilon=\phi$ = 0.45	$\varepsilon=\phi$ = 0.46
ψ = 111 erg/cm^3 sec	ψ = 140	ψ = 126	ψ = 254	ψ = 301	ψ = 603	ψ = 2965
d_{32} = 0.21 cm	d_{32} = 0.19	d_{32} = 0.20	d_{32} = 0.15	d_{32} = 0.14	d_{32} = 0.11	d_{32} = 0.056
$a = \frac{6\varepsilon}{d_{32}}$ = 12.0 cm^{-1}	a = 12.0	a = 12.0	a = 15.2	a = 18.86	a = 24.55	a = 49
1.2	0.95	1.1	0.65	0.51	0.35	0.08
$\frac{Re}{p^{0.15}}$ = 1.2						
v_t = 2.93 cm/sec	v_t = 2.56	v_t = 2.82	v_t = 2.22	v_t = 1.86	v_t = 1.63	v_t = 0.73
k_c = 0.0101 cm/sec	k_c = 0.0099	k_c = 0.0101	k_c = 0.0104	k_c = 0.0098	k_c = 0.0104	k_c = 0.0097
k_d = 0.0100 cm/sec	k_d = 0.0087	k_d = 0.0096	k_d = 0.0075	k_d = 0.0063	k_d = 0.0056	k_d = 0.0025
K_c = 0.005 cm/sec	K_c = 0.0047	K_c = 0.0049	K_c = 0.0044	K_c = 0.0039	K_c = 0.0037	K_c = 0.002
H_x = 8.83 cm	H_x = 9.40	H_x = 9.01	H_x = 6.13	H_x = 4.49	H_x = 2.75	H_x = 1.22
E_c = 1.76 cm^2/sec	E_c = 1.53	E_c = 1.13	E_c = 2.15	E_c = 2.24	E_c = 2.65	E_c = 3.91
Assume $E_c = E_d$						
$\left(\frac{E_c}{U_c}\right)$ 3.32 cm	2.89	2.13	5.24	6.79	10.60	32.58
$\left(\frac{E_d}{U_d}\right)$ 6.29 cm	5.46	4.04	9.77	12.44	20.38	55.86
H_x' 11.37 cm	9.88	9.30	17.16	21.47	33.63	92.35

$$H_x = \frac{U_c}{K_c a} \qquad (12)$$

This value does not take axial dispersion into account. To find the axial dispersion coefficient, E, Baird has found the following equation to be effective for 2 in. columns [Ref. 52].

$$E_c = 5.62\ a^{1.41}\ f^{0.73}\ H^{-0.88} \qquad (13)$$

It has also been shown that the assumption of $E_c = E_d$ is valid [Ref. 46].

So the height of a transfer unit taking axial dispersion into effect can be found by Equation 14 [Ref. 53].

$$H_x' = H_x + \frac{E_c}{U_c} + \frac{E_d}{U_d} \qquad (14)$$

By examining Table II-9, it can be seen that the best H_x occur when the flows are low and agitation high. But when the axial dispersion is taken into account, the H_x' appears to be best in the low flow situation. The next step in the evaluation of the Karr column is to measure the mass transfer and axial dispersion to confirm these results.

NOMENCLATURE

a 1/2 stroke amplitude, cm

A Stroke amplitude (top to bottom), cm

C_o Discharge coefficient, dimensionless

d_{32} Sauter mean drop diameter, cm

D Diffusivity, $\frac{cm^2}{sec}$

E Axial dispersion coefficient, cm^2/sec

f Frequency, cycles/sec

g Acceleration due to gravity, 981 cm/sec^2

h Plate spacing, cm

H Height of a transfer unit, cm

k Mass transfer coefficient in one phase, $\frac{cm}{sec}$

K_c Overall mass transfer coefficient, cm

L $\frac{U_d}{U_c}$, dimensionless

m Distribution ratio, dimensionless

Re Reynolds number $\frac{d\ v_t\ \rho_c}{\mu_c}$, dimensionless

S_c Schmidt number $\frac{\mu}{\rho D}$, dimensionless

Sh Sherwood number $\frac{k_c\ d_{32}}{D}$, dimensionless

U Superficial velocity, $\frac{cm}{sec}$

v_t Terminal velocity, cm/sec

Greek Letters

γ Interfacial tension, $\frac{dyne}{cm}$

ε Volume fraction of dispersed phase, dimensionless

μ Viscosity poise, dimensionless

ρ Density, g/cm^3

$\bar{\rho}$ Average density = $(\varepsilon P_d + (1-\varepsilon) P_c)$, g/cm^3

ψ Energy dissipation per unit volume, $erg/cm^3 sec$

σ Fraction open area of plate, dimensionless

Subscripts

c Continuous phase

d Dispersed phase

f Flooding

s Slip value

III. Metal hydride studies

Jahn-Teller resonance states in the Vb metal hydrides: static and dynamic consequences

G. C. Abell

INTRODUCTION

The concept of Jahn-Teller (JT) resonance states was recently introduced to explain the unusual behavior of hydrogen in the Vb metals (V, Nb and Ta) [Ref. 1]. This idea seemed to make a strong connection to experimental facts, but as presented it was largely qualitative; moreover, the question of plausibility was unresolved. This latter problem was settled by a model calculation using a simple tight-binding (TB) Hamiltonian for the metal d-band [Ref. 2]. One interesting result of that study was the similarity of the full Hamiltonian (JT state interacting with d-band) to the Anderson Hamiltonian for magnetic impurities in metals [Ref. 3]. The purpose of the present paper is to exploit that similarity, taking advantage of the fact that this latter Hamiltonian, including both static and dynamic effects, is reasonably well understood. In particular, we describe a Hartree-Fock (HF) approximation and discuss conditions under which JT resonance stabilization can occur. We argue that interstitial hydrogen acts indirectly to trigger an instability in the adjacent JT orbital. The idea of a relatively sharp boundary separating different regions in the HF parameter space is discussed in the context of dynamical effects, and the likelihood of a low temperature Kondo anomaly is briefly considered. Then, likely relaxation mechanisms are described and an expression is given for the susceptibility corresponding to one of these. This particular mechanism quantitatively explains a dispersion step observed in an acoustic phonon branch of both NbH_x and TaH_x [Ref. 4].

THE SINGLE IMPURITY JT HAMILTONIAN

Before writing down the Hamiltonian, it will be useful to reiterate the basic hypothesis developed in Reference 1 and 2. In the Vb metals there is a degenerate molecular orbital, $\phi^{\pm}_{JT}$, made up of atomic t_{2g} d-orbitals belonging to the four-atom metal cluster surrounding a given t-site. This degenerate orbital has a localized JT electron-phonon interaction comparable to its band-coupling interaction. Band-coupling quenches the JT degeneracy in the pure metal; whereas in the hydride, occupancy of the t-site by hydrogen tips the scales in favor of a localized symmetry-lowering distortion of the occupied cluster. This is the instability referred to in the previous section. Because hydrogen directly affects only the fully symmetric subspace, its role is indirect (see Reference 2 for a more complete discussion of this point). Thus, the following treatment does not explicitly include the hydrogen potential. The Hamiltonian for a single JT defect in second-quantitized notation is ($\hbar$ = 1 throughout the text)

$$H = \sum_k \varepsilon_k n_k + \varepsilon_o (n_+ + n_-) + V\left[\sum_{\sigma=\pm}(\psi_\sigma^\dagger c_\sigma + H.C.)\right] + \lambda(n_+ - n_-)(b^\dagger + b) + \omega_o b^\dagger b. \quad (1)$$

The first term describes band electrons; the fermion operators $c_k^\dagger(c_k)$ create (destroy) particles in orbitals $|k\rangle$ of a noninteracting Fermi gas with $n_k \equiv c_k^\dagger c_k$ the number

operator (electron spin has been suppressed so that $o \leq n \leq 2$). The second term represents the JT defect; $c_{\pm}^{\dagger}$ creates a particle in the JT orbital $\phi_{JT}^{\pm}$, which is orthogonal to the $|k>$. The third term represents the band-coupling interaction; V is a hopping matrix element connecting the JT orbital and $\psi_{\pm}^{\dagger}$, a local combination of the $|k>$ having the same point symmetry as $c_{\pm}^{\dagger}$ (the index $\sigma=\pm$ labels the appropriate real basis of the doubly degenerate E representation belonging to the D_{2d} point group of a t-site). The fourth term is the JT electron-phonon interaction; λ is the coupling constant, $b^{\dagger}$ is the phonon creation operator for the relevant local mode and $(b^{\dagger}+b)$ is the JT-active displacement. The last term is the kinetic energy of the local oscillator, with frequency ω_o.

THE SLOW JT HAMILTONIAN

To gain some insight into the behavior of the full Hamiltonian (1), we invoke the Born-Oppenheimer (BO) approximation that the electrons adjust adiabatically to the instantaneous defect nuclear configuration. As was pointed out in Reference 2, this is a good approximation in the isolated molecular (V=O) limit for Exβ JT coupling [Ref. 5]. For finite V, the approximation necessarily breaks down at low enough temperatures because of the orthogonality catastrophe theorem [Ref. 6 and 7]. For now, we assume that there is a region of validity for the BO approximation, deferring until later a discussion of the low-temperature (Kondo) problem. The following is an HF type of theory [Ref. 8]. The operator (n_+-n_-) of Hamiltonian (1) is replaced by its expectation value $S \equiv <n_+-n_->$ to calculate the boson states. Using a simple displaced oscillator transformation, the bose operators for the new ground state are found to be $a^{\dagger} = b^{\dagger} + \lambda S/\omega_o$ and its conjugate. An effective one-electron Hamiltonian is now obtained by replacing $(b^{\dagger} + b)$ by its expectation value

$$<b^{\dagger} + b> = -(2\lambda/\omega_o)S \qquad (2)$$

giving:

$$\tilde{H} = \sum_k \varepsilon_k n_k + V\left[\sum_{\sigma=\pm}(\psi_\sigma^{\dagger}c_\sigma + H.C.)\right] + \varepsilon_+ n_+ + \varepsilon_- n_- + \tfrac{1}{2}\varepsilon_{JT}S^2 + \omega_o a^{\dagger}a. \qquad (3)$$

In this expression

$$\varepsilon_{\pm} = \varepsilon_o \mp \varepsilon_{JT}S, \qquad (4)$$

where $\varepsilon_{JT} \equiv 2\lambda^2/\omega_o$ and $a^{\dagger} + a$ has been replaced by its expectation value of zero.

Apart from the oscillator energy, Hamiltonian (3) – which because of approximation (2) is only valid for low frequencies ($\omega << \omega_o$) – is essentially the same as the HF approximation to the Anderson Hamiltonian for magnetic impurities in metals [Ref. 3]. The HF method of solution is to calculate self-consistent values of $S \equiv <n_+-n_->$, using a Green's function formalism with some particular modeling of the free-electron (band) states and of the band-coupling term proportional to V. There are two distinct solutions; a nondegenerate one corresponding to S=O and a doubly dengerate one with $S=\pm p$, where p is a positive number satisfying $p_c \leq p \leq 2$. The non-degenerate solution always gives self-consistency, but the degenerate solution is the stable one if it exists. In the present case, $S \neq 0$ corresponds to orbital, rather than to spin-polarization. Thus, S is fully analogous to electron spin and will be called pseudospin. Some examples of the above HF treatment are given in References 2 and 8. A more general approach within the HF scheme is given in Reference 7.

The results are most succinctly expressed in terms of an HF 'phase diagram' in the parameter space. The important parameters for the low-frequency Hamiltonian (3) are, in reduced form:

$$\varepsilon_r \equiv (\varepsilon_F - \varepsilon_o)/\varepsilon_{JT},$$

$$V_r \equiv V/\varepsilon_{JT}, \qquad (5)$$

where ε_F is the Fermi level. Figure III-1 is a schematic HF phase diagram in (ε_r, V_r)-space showing regions of broken symmetry HF solutions ($S=\pm p$) and of quenched HF solutions ($S=0$). The use of the term "quenched" refers to the fact that for sufficiently large V_r, the kinetic energy stabilization from band-coupling overwhelms the local JT energy gain.

Figure III-1 also illustrates the role of hydrogen: in the pure Vb metals (represented by Nb), the JT degeneracy is quenched. When a single hydrogen impurity occupies a t-site in Nb, the self-energy ε_o of the JT orbital belonging to the occupied cluster is renormalized (see Reference 2), forcing the system across the boundary. Quite apart from the details, this role of hydrogen – indirect though it may be – is essential to the integrity of the concept of JT resonance states as applied to the Vb hydrides [Ref. 1 and 2].

It should be emphasized here that in the case of the impurity problem, sharp boundaries like those of Figure III-1 are artifacts of mean-field theory [Ref. 7]. In particular, the broken-symmetry region of Figure III-1 is a Kondo regime involving exotic many-body effects [Ref. 9]. In fact, if Hamiltonian (3) mapped fully onto the Anderson Hamiltonian for magnetic impurities, then – given that $\varepsilon_{JT} \sim V$ [~(1eV); see Reference 2] corresponding to an intermediate-coupling Anderson model – the broken

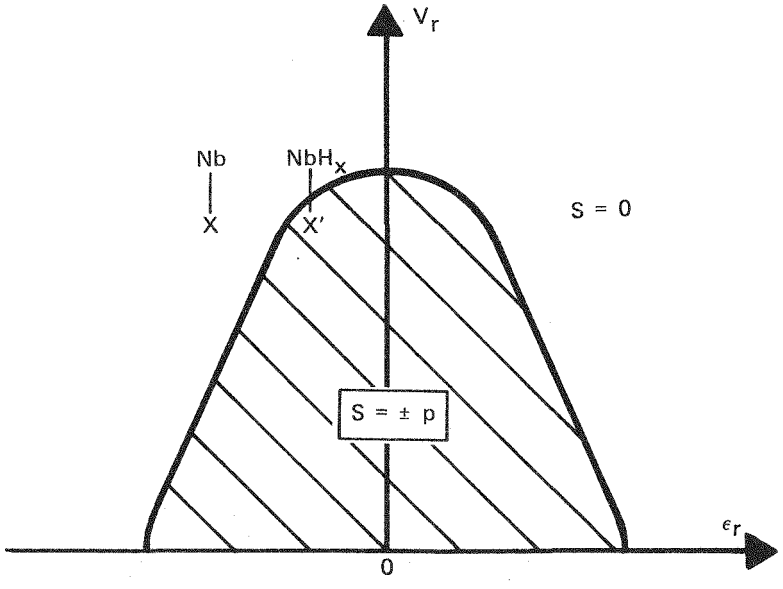

FIGURE III-1 - Hartree-Fock 'phase diagram' in reduced parameter space (schematic).

symmetry solutions would have little physical significance. This is so because of a very large Kondo temperature in such a case, $T_K \simeq 10^4$K (the significance of T_K is that symmetry invariance is restored on a time scale given by its inverse) [Ref. 7]. It is questionable whether the JT coupling could have observable consequences if that were the case. But as stated earlier, Hamiltonian (3) is only valid for low frequency excitations, $\omega << \omega_o$. The spin-flip excitations (involving the pseudo-spin S), which give rise to Kondo-quenching, correspond in the present case to transitions between degenerate vibronic states, in which not only electronic but also nuclear spatial coordinates must be 'flipped.' The Kondo problem for such a case remains to be worked out, but results will probably be quite different from the traditional Kondo problem. It is likely that conduction electron and phonon scattering will both play an important role. Given the vibronic character of the relevant exchange scattering, we propose that the basic scale (cutoff) determining T_K is ω[$\sim$100 K]. This suggests that a low-temperature resistivity study of a dilute solid-solution phase Vb hydride might show a Kondo minimum. Moreover, it suggests that the possibility of dramatic effects implied by the phase boundary shown in Figure III-1 is a real one, at least at normal temperatures

ANELASTIC RELAXATION MECHANISMS

The purpose of this section is to study the response of an ensemble of hydrogen-induced JT defects to an externally imposed elastic tetragonal deformation. Experimentally, such a deformation is achieved by exciting the T_1A phonon branch, using either neutron scattering or ultrasonic methods. In fact, the existence of a dispersion step in the T_1A branch between ultrasonic (10^7Hz) and neutron (10^{12}Hz) frequencies in both NbH_x and TaH_x implicates a relaxation mechanism in this frequency range [Ref. 4]. There are two distinct slow relaxation mechanisms implied by the JT Hamiltonian (3). To describe these, we schematize in Figure III-2 the effect of a tetragonal strain (represented by the arrows) on the JT orbitals $\phi^{\pm}_{JT}$ and on the corresponding local density of states (DOS) $\rho\pm$, which is the projection of total DOS onto $\phi^{\pm}_{JT}$. The $\phi^{\pm}_{JT}$ are shown as particular combinations of atomic orbitals, represented by the circles, with solid and dashed lines corresponding to opposite phases. In the lower part of the figure, the deformation is seen to diminish overlap along bonding directions (atomic orbitals out of phase). This destabilizes $\phi^{\pm}_{JT}$ by an amount $z = e\beta$, where e is the magnitude of the strain and β is the strain coupling coefficient. The local DOS ρ^+ is displaced upward by the same amount. The effect on ϕ^{-}_{JT} and ρ_- shown in the upper part of Figure III-2 is in the opposite direction (stabilizing). This adiabatic displacement of ρ_+ and ρ_- changes the relative occupancy S of the two states. But according to Equations (3) and (4), the system must undergo a further change in S to restore self-consistency. This latter relaxation, which we call isoconformational, constitutes a slow (anelastic) response to the strain field, with a characteristic frequency directly related to ω_o. By contrast, 'free' electrons follow the perturbation adiabatically. Before presenting an expression for this slow response, we consider briefly another mechanism -- reorientation relaxation. To see this, take the vertical and horizontal directions of Figure III-2 as the y and x axes of the lattice. Then the JT defect shown in Figure III-2 may be called

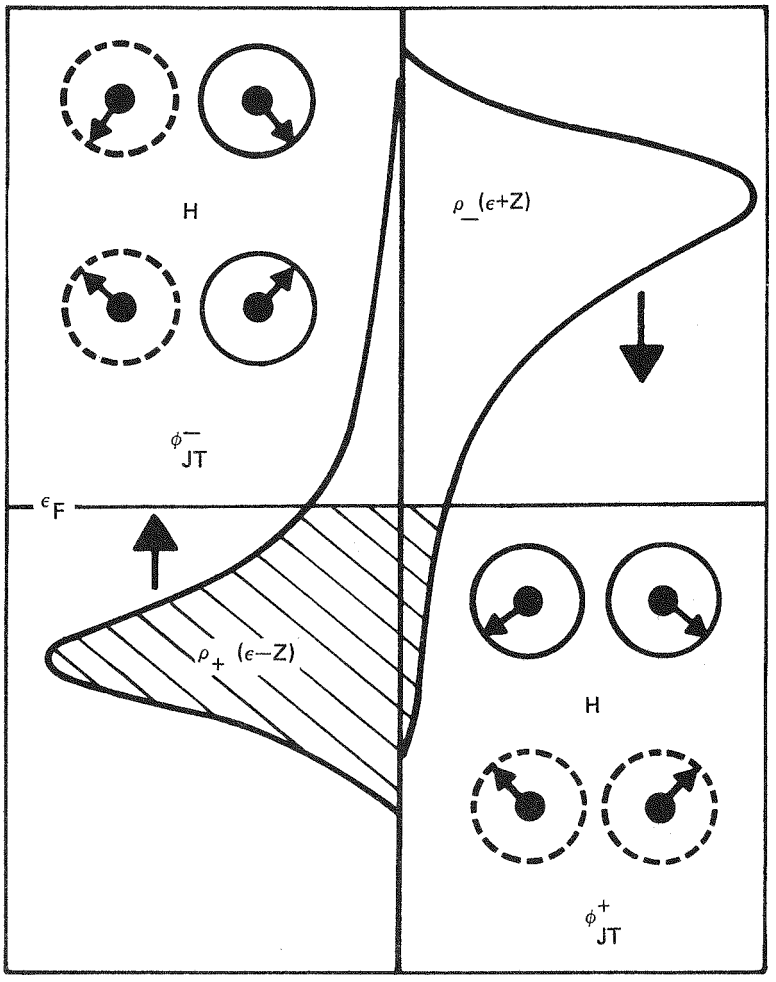

FIGURE III-2 - Effect of tetragonal strain on $\phi^{\pm}_{JT}$ and $\rho_{\pm}$ (schematic).

a y-type defect, because the axis of enlongation is along y. Clearly, this same JT defect could have been shown with its axis of enlongation along x, in which case it would be x-type. Notice, however, that the external strain field affects the two types oppositely: an x-type defect would have ϕ^-_{JT} rather than ϕ^+_{JT} lowest in energy and the relative displacements of the local DOS would be opposite to that shown in Figure III-2. The net effect is that x-types would be stabilized relative to y-types. The system could take advantage of that via reorientation relaxation, limited by the balance between free energy gain and entropy loss. Considered naively, this would predict a 1/T temperature dependence for the relaxation. It must be remembered though, that these JT defects are strongly coupled to the Fermi gas (V is large) -- they are not free to reorient as isolated entities. Because reorientation relaxation involves flipping the pseudo-spin S, it is intimately related to the Kondo problem referred to earlier, and thus cannot be treated independently of the electron gas. We will ignore reorientation relaxation, leaving the problem unresolved for now.

In the case of isoconformational relaxation, there is no pseudo-spin flip, and the defect may be treated independently of the electron gas. We have derived the following expression for the static and high frequency limits of the elastic susceptibility due to this latter mechanism:

(a) $\omega << \omega_o$,

$$\chi_o = 2\rho_{JT}\beta^2/(1-2\rho_{JT}\varepsilon_{JT}); \text{ and} \quad (6a)$$

(b) $\omega >> \omega_o$,

$$\chi_\infty = 2\rho_{JT}\beta^2, \quad (6b)$$

where $\rho_{JT} \equiv \rho_+(\varepsilon_F) + \rho_-(\varepsilon_F)$. This result requires no special assumptions beyond those already contained in Hamiltonian (3). Note that when S=0, $\rho_{JT} = 2\rho_o(\varepsilon_F)$ (i.e., $\rho_+ = \rho_- = \rho_o$), where ρ_o is the local DOS projected into $\phi^{\pm}_{JT}$ for the unperturbed (quenched) system. Thus, in the quenched case, the denominator of equation (6a) diverges when $4\varepsilon_{JT}\rho_o(\varepsilon_F) = 1$, and this relation determines the phase boundary illustrated in Figure III-1.

We now show that the isoconformational relaxation can explain the dispersion step observed in the T_1A phonon branch of NbH_x and TaH_x, referred to earlier. First, we relate the susceptibility (6) to a difference in the T_1A elastic constant $C' \equiv \frac{1}{2}(C_{11}-C_{12})$ for a given hydrogen composition, between its value measured at 10^{12}Hz (neutron diffraction) and that at 10^7Hz (ultrasonic). Assuming that the characteristic frequency of the isoconformational relaxation mechanism lies well with this range,

$$\Delta C'_{relax} \equiv [C'(10^{12}\text{Hz}) - C'(10^7\text{Hz})]_{MH_x}$$
$$= -\tfrac{1}{3}N_H(\chi_\infty - \chi_o) \quad (7)$$

where N_H is the hydrogen concentration (which is also the concentration of JT defects) and the factor $\frac{1}{3}$ is required because only one of the three types (x-, y- and z-) of t-sites are affected by a particular <110> shear strain. In Equation (7) we have used the relations $E = E_o - e^2\chi N_H$ and $C' \equiv (E-E_o)/e^2$. The observed dispersion step [Ref. 4] is given in terms of $\Delta\nu/\nu_M$ vs. k(110), where $\Delta\nu$ is the frequency of the hydride relative to ν_M, the frequency of the pure metal. Using the relation $C \propto \nu^2/k^2$ (valid for small k) and the fact that $\Delta\nu << \nu_M$ gives $(C'_{MH_x} - C'_M)/C'_M \simeq 2\Delta\nu/\nu_M$. Since there is no dispersion step for the pure metal, the observed relaxation is:

$$\Delta C'_{relax} = 2C'_M \left(\lim_{k\to 0}[(\Delta\nu/\nu_M)_{neu.diff.} - (\Delta\nu/\nu_M)_{ultras.}]_{MH_x}\right) \quad (8)$$

Precise determination of the susceptibility (6) requires knowledge of β, ρ_{JT}, and ε_{JT}. Given that the system is reasonably close to the boundary (see the discussion of Figure III-1) such that $2\rho_{JT}\varepsilon_{JT} \lesssim 1$, a resonable estimate may be obtained by taking $\rho_{JT} = (4\varepsilon_{JT})^{-1}$. This latter value is close to values of ρ_{JT} obtained in model calculations [Ref. 2] and gives $\chi_\infty - \chi_o = -\beta^2/2\varepsilon_{JT}$. Since $\beta \simeq \lambda \cdot R$ and $\varepsilon_{JT} = \lambda^2/2\mu\omega_o^2$ [Ref. 10], where $R \simeq 3A$ is the nearest-neighbor distance, and μ is the mass of a cluster metal atom; we obtain $\chi_\infty - \chi_o \simeq -\mu\omega_o^2R^2$. It was proposed in Reference 2 that a dispersionless excitation observed in a neutron scattering study of α-phase $NbH_{0.8}$ [Ref. 11] at $\omega \simeq 10^{-2}$eV corresponds to a transition between oscillator levels of the JT quasiparticle (or, more accurately, quasimolecule). Taking this value for ω_o gives $\chi_\infty - \chi_o \simeq -22$eV and by Equation (7) the calculated isoconformational relaxation for NbH_x is $\Delta C'_{relax}$(per 1% H) = 0.6×10^{10} erg cm^{-3}. The observed relaxation, given by Equation (8) (adjusted to $N_H = 5 \times 10^{20}$ cm^{-3} = 1% H, and using $C'_M = 55 \times 10^{10}$ erg cm^{-3}) [Ref. 12] is $\Delta C'_{relax}$(per 1% H) = 0.4×10^{10} erg cm^{-3} for NbH_x and only slightly larger for TaH_x. In addition to this numerical agreement, the theory

also predicts by Equation (6) and (7) that $\Delta C'_{relax}$ should be temperature-independent, as observed [Ref. 12]. This temperature independence is a consequence of the Fermi statistics and can be understood in essentially the same way as that of the magnetic susceptibility of conduction electrons [Ref. 13]. In spite of the above agreement, the theory must be considered incomplete until the previously discussed Kondo problem and the related issue of reorientation relaxation are resolved.

SUMMARY AND DISCUSSION

The Hamiltonian for a single JT impurity was shown, in a certain approximation, to be formally the same as the Anderson Hamiltonian for magnetic impurities in metals. Based on this similarity, a Hartree-Fock 'phase diagram' was described and used to explain the role of hydrogen in triggering the JT instability. Relaxation mechanisms for the JT defect were described. The elastic susceptibility due to one of these was discussed and shown to be consistent with the magnitude and temperature dependence of an observed phonon relaxation. The other relaxation was shown to be a Kondo problem, suggesting that Kondo anomalies might exist in the low-temperature behavior of suitable Vb hydrides.

Clearly, some important questions remain to be answered. Thus, until the JT-Kondo problem is resolved, the importance of reorientation relaxation cannot be assessed. A related issue is the physical significance of the 'phase diagram' shown in Figure III-1. It is well-known that the broken symmetry regime cannot be a true ground state [Ref. 7], so it is important to determine the temperature range over which the present HF description is valid. Any attempt to revolve these issues must take into account the very substantial difference between the JT-Kondo problem and the traditional one. In the latter case the exchange scattering involves only electronic coordinates; in the JT case, nuclear coordinates are intimately involved as well. The spin-flip is vibronic rather than electronic.

The most important question, though, has to do with the very nature of the JT electron-phonon interaction. First of all, it exists already in the host metal -- as we have often emphasized, the role of hydrogen is indirect. Second, it is a strongly localized interaction, confined to the four-atom cluster around a given t-site. If one starts with the usual representation (based on the BO approximation and the periodic lattice assumption) of Bloch waves for electrons and lattice vibrations for phonons, then it is very difficult to see how the JT electron-phonon interaction could arise. In fact, JT distortion represents a breakdown of the BO approximation, so that the usual descriptive basis must necessarily fail in such a case. In transition metals, TB theory has been successfully used to discuss electron-phonon interactions [Ref. 14]. A key parameter is the dependence of the hopping energy V on nearest neighbor separation. But the atomic TB basis is not really a natural representation for describing resonance due to electron-phonon coupling. Local vibrations are not a property of individual atoms, but of groups of atoms. Thus, if we wish to consider some localized entity that vibrates, we must conceptualize to molecules rather than to atoms. The solid may always be partitioned

into molecular units (e.g., diatoms), but such an approach may be seen as introducing unnecessary complications; moreover, the crystallographer may argue that this partitioning has no empirical basis in the case of pure transition metals. Nonetheless, if it can be shown that a particular grouping exhibits an unusually large local interaction, then localization may well be a possibility. (By local interaction, we mean the effect of a local (molecular) vibrational mode on a 'site' energy of one of the molecular 'TB' orbitals.) But why should the orbital ϕ_{JT}, belonging to the four-atom cluster of the t-site, be special in this regard? One could partition the lattice in other ways giving one or more degenerate molecular orbitals lying close to the Fermi level, again with the possibility of JT stabilization. Nonetheless, we believe that the particular molecular orbital ϕ_{JT}, together with its electron-phonon interaction, is indeed special. It is an instance of the famous four-atom, four-electron problem paradiagmatically represented by the four-center exchange reaction $H_2+D_2 \rightleftarrows 2HD$, which is a prime example of the controlling importance of orbital symmetry in chemical reactions [Ref. 15 and 16]. That highly symmetric structures of a four-atom, four-electron system are unstable by eV amounts (the energy of a covalent bond) with respect to symmetry-lowering rearrangements is an established fact of chemistry. The effect is theoretically understood for the H_4 problem at the level of sophisticated *ab initio* quantum-mechanical calculations [Ref. 17 and 18]. In the larger class of highly symmetric n-atom clusters (which will be referred to loosely as ring-of-n), the ring-of-four is the leading member of an alternating sequence in which symmetric structures with 4k electrons are unstable, while those with 4k+2 electrons (e.g., the π-electrons of benzene) are stable [Ref. 19]. The four-electron ring-of-four structure is by far the most unstable of these, thus explaining the special character of ϕ_{JT}. In this context, localization in TB solids due to intramolecular 'ring-of-four' orbital repulsion should be no more surprising than that due to intraatomic Coulombic spin repulsion. The Mott insulator is a well-known example of localization at every site, without randomness, due to Coulombic interactions [Ref. 9]. By analogy, we suggest that insulating condensed hydrogen is an example of molecular localization due to the intramolecular 'ring-of-four' repulsion. In other words, it is this latter interaction rather than Coulombic repulsion which inhibits the formation of metallic hydrogen.

Reference

I. Low temperature research

1. Mound Facility Activities in Chemical and Physical Research: January-June 1980, MLM-2756 (August 29, 1980), pp. 15-16.

2. Mound Facility Activities in Chemical and Physical Research: January-June 1981, MLM-2884 (December 15, 1981), pp. 6-11.

3. R. D. Evans, The Atomic Nucleus, McGraw-Hill, New York, 1955, pp. 611-613.

4. Mound Facility Activities in Chemical and Physical Research: July-December 1980, MLM-2809 (April 10, 1981), pp. 6-8.

5. E. R. Grilly, J. Am. Chem. Soc., 73, 843 (1951).

6. H. R. Woolley, R. B. Scott, and F. G. Brickwedde, J. Res. Natl. Bur. Stand., 41, 379 (1948).

7. G. T. McConville and D. White, Physica B+C, 108, 271 (1981).

8. E. Wigner, Phys. Rev., 40, 749 (1932).

9. J. G. Kirkwood, Phys. Rev., 44, 31 (1933).

10. R. D. Etters, R. Danilowicz, and W. England, Phys. Rev., A12, 2199 (1975).

11. G. T. McConville, J. Chem. Phys., 74, 2201 (1981).

II. Separation research

1. G. P. Flynn, R. V. Hanks, N. A. Lemaire, and J. Ross, J. Chem. Phys., 30, 154 (19630.

2. J. T. K. Kao, W. Ruska, and R. Kobayashi, Rev. Sci. Instru., 39, 824 (1968).

3. S. B. K. Sun and T. S. Storvick, J. Chem. Eng. Data, 24, 88 (1979).

4. J. Kestin, S. T. Ro, and W. A. Wakeham, J. Chem. Phys., 56, 4119 (1972).

5. J. Kestin and W. Leidenfrost, Physica, 25, 1033 (1959).

6. M. de Haas, Comm. Leiden No. 12, (1894).

7. H. Stakelbeck, Z. Ges. Kalte - Ind., 40, 33 (1933).

8. A. F. Benning and W. H. Markwood, Jr., Refrig. Eng., 37, 243 (1939).

9. J. H. Awbery and E. Griffiths, Proc. Phys. Soc., (London) 48, 372 (1936).

10. W. M. Rutherford and K. W. Laughlin, Science, 211, 1054 (1981).

11. V. M. Loyola, R. G. Wilkins, and R. Pizer, "The Kinetics of Complexing of Calcium Ions with Several Cryptands," J. Am. Chem. Soc., 97, 7382 (1975).

12. Mound Facility Activities in Chemical and Physical Research: July-December 1980, MLM-2809 (April 10, 1981), pp. 28-30.

13. Mound Facility Activities in Chemical and Physical Research: January-June 1981, MLM-2884 (December 15, 1981), pp. 25-27.

14. T. R. Marrero and E. A. Mason, J. Phys. Chem. Ref. Data, 1, 3 (1972); T. R. Marrero and E. A. Mason, Advances in Atomic and Molecular Physics, (Academic, New York, 1970), Vol. 6 Chapter 4, p. 156.

15. P. S. Arora, H. L. Robjohns, and P. J. Dunlop, Physica, 95A, 561 (1979).

16. W. Hogervorst, Physica, 51, 59 (1971).

17. C. J. Zwakhals and K. W. Reus, Physica, 1006, 231 (1980).

18. B. A. Kalinin and P. E. Suetin, Heat Transfer-Sov. Res., 7, 146 (1975).

19. P. E. Suetin, B. A. Kalinin, and A. E. Loiko, Sov. Phys.-Tech. Phys., 15, 1349 (1971).

20. J. C. Liner and S. Weissman, J. Chem. Phys., 56, 2288 (1972).

21. V. P. S. Nain and S. C. Saxena, Appl. Sci. Res., 23, 121 (1970).

22. A. E. Loiko, B. A. Ivakin, and P. E. Suetin, Sov. Phys.-Tech. Phys., 19, 434 (1974).

23. R. A. Aziz, P. W. Riley, U. Buck, G. Maneke, J. Schleusener, G. Scoles, and U. Valbusa, J. Chem. Phys., 71, 2637 (1979).

24. Mound Facility Activities in Chemical and Physical Research: January-June 1980, MLM-2756 (August 29, 1980), pp. 35-47.

25. W. L. Taylor, J. Chem. Phys., 72, 4973 (1980).

26. J. H. Dymond and B. J. Alder, J. Chem. Phys., 51, 309 (1969).

27. H. M. Lin and R. L. Robinson, Jr., J. Chem. Phys., 54, 52 (1971).

28. C. H. Chen, P. E. Siska, and Y. T. Lee, J. Chem. Phys., 59, 601 (1973).

29. E. A. Mason and W. E. Rice, J. Chem. Phys., 22, 843 (1954).

30. R. Ahlrich, R. Penco, and G. Scoles, J. Chem. Phys., 19, 119 (1977).

31. R. W. York, W. L. Taylor, P. T. Pickett, and R. E. Miers, "Low Energy Total Cross Sections for the Argon-Krypton System," Progress in Astronautics and Aeronautics, Vol. 51, Part II, 1977, pp. 1075-1089.

32. W. L. Taylor, R. W. York, and P. T. Pickett, "Velocity Dependences of Low-Energy Neon-Argon Total Cross Sections," Progress in Astronautics and Aeronautics, Vol. 74, Part II, 1981, pp. 895-911.

33. Mound Facility Activities in Chemical and Physical Research: July-December 1980, MLM-2809 (April 10, 1981), pp. 31-37.

34. F. Pirani and F. Vecchiocattivi, J. Chem. Phys., 66, 372 (1977).

35. J. H. Dymond and B. J. Alder, J. Chem. Phys., 51, 309 (1969).

36. H. M. Lin and R. L. Robinson, Jr., J. Chem. Phys., 54, 52 (1971).

37. E. A. Mason and W. E. Rice, J. Chem. Phys., 22, 843 (1954).

38. C. H. Chen, P. E. Siska, and Y. T. Lee, J. Chem. Phys., 59, 601 (1973).

39. R. A. Aziz, P. W. Riley, U. Buck, G. Maneke, J. Schleusener, G. Scoles, and U. Valbusa, J. Chem. Phys., 71, 2637 (1979).

40. P. S. Arora, H. L. Robjohns, and P. J. Dunlop, Physica, 95A, 561 (1979).

41. G. C. Maitland and W. A. Wakeham, Mol. Phys., 35, 1443 (1978).

42. M. Keil, J. T. Slankas, and A. Kuppermann, J. Chem. Phys., 70, 482 (1979).

43. A. E. Karr, AIChe J., 5, 446 (1959).

44. M. M. Hafez, M. H. I. Baird, I. Nirdosh, Can. J. Chem. Eng., 57, 150 (1979).

45. J. D. Thornton, Chem. Eng. Sci., 5, 201 (1956).

46. M. M. Hafez, M. H. I. Baird, I. Nirdosh, presented at the International Solvent Extract Conference, Liege, Belgium, Sept. 6-12, 1980.

47. A. C. Jealous and H. F. Johnson, Ind. Eng. Chem., 47, 1159 (1955).

48. M. M. Hafez and M. H. I. Baird, Trans. I. Chem. Eng. (London), 56, 229, (1978).

49. G. S. Ladda and T. E. Degaleesan, Transport Phenomena in Liquid Extraction, McGraw-Hill, 1978, pp. 187, 191.

50. R. E. Treybal, Liquid Extraction, 2nd Ed., McGraw-Hill, 1963, p. 185.

51. B. E. Jepson and R. DeWitt, J. Inorg. Nucl. Chem., 38, 1175 (1976).

52. S. D. Kim and M. H. I. Baird, Can. J. Chem. Eng., 54, 81 (1976).

53. C. Hanson, Recent Advances in Liquid-Liquid Extraction, Pergammon, 1971, p. 230.

III. Metal hydride studies

1. G. C. Abell, Phys. Rev. B, 20, 4773-4788 (1979).

2. G. C. Abell, Phys. Rev. B, 22, 2014-2019 (1980).

3. P. W. Anderson, Phys. Rev., 124, 41 (1961).

4. A. Magarl, et al., J. Phys. C, 11, 2175-2181 (1978).

5. H. Thomas, Electron-Phonon Interactions and Phase Transitions, Plenum, New York, 1977, pp. 245-270.

6. P. W. Anderson, Phys. Rev. Lett., 18, 1049 (1967).

7. F. D. M. Haldane, Phys. Rev. B, 15, 281-289 (1977).

8. A. C. Hewson and D. M. Newns, J. Phys. C, 12, 1665-1683 (1979).

9. P. W. Anderson, Rev. Mod. Phys., 50, 191-201 (1978).

10. F. S. Ham, Electron Paramagnetic Resonance, Plenum, New York, 1972, pp. 1-119.

11. S. M. Shapiro, et al., Phys. Rev. Lett., 41, 1051 (1978).

12. A. Magerl, et al., Phys. Stat. Sol (a), 36, 161-171 (1976).

13. C. Kittel, Introduction to Solid State Physics, 4th Ed., John Wiley, New York, 1971.

14. C. M. Varma and W. Weber, Phys. Rev. B, 19, 6142-6154 (1979).

15. R. Hoffman and R. B. Woodward, Science, 167, 825-831 (1970).

16. W. A. Goddard III, J. Am. Chem. Soc., 94, 793-807 (1972).

17. W. Gerhartz, J. Am. Chem. Soc., 99, 4263-4271 (1977).

18. J. D. Goddard and I. G. Csizmadia, Chem. Phys. Lett., 64, 219 (1979).

19. J. Aihara, Bull. Chem. Soc. Japan, 48, 517 (1975).

DO NOT MICROFILM

Distribution

EXTERNAL

TIC-4500, UC-4 and UC-22 (194)
H. N Hill, DOE/Dayton Area Office
E. L. Venturini, Sandia National Laboratories, Albuquerque
R. K. Flitcraft, Monsanto Research Corporation
F. D. Stevenson, DOE/Office of Basic Energy Sciences
J. Burnett, DOE/Office of Basic Energy Sciences
N. Haberman, DOE/Division of Nuclear Energy
J. R. Blair, DOE/Office of Health and Environmental Research
J. N. Maddox, DOE/Office of Health and Environmental Research
D. White, University of Pennsylvania
Monsanto Reports Library, R2C, St. Louis

INTERNAL

G. C. Abell
W. R. Amos
L. R. Baird
R. C. Bowman
D. Cain
W. T. Cave
R. E. Ellefson
C. W. Huntington
B. E. Jepson
G. T. McConville
D. A. Menke
E. D. Michaels
W. M. Rutherford
G. C. Shockey
G. L. Silver
W. L. Taylor
R. E. Vallee
W. R. Wilkes
L. J. Wittenberg
R. W. York
Document Control
Library (15)
Publications

Published by Information Services:
Stephen L. Nowka, Editor